Minimum-Excess-Work Guidance

Christopher Kolloff [*1 2] **Tobias Höppe** [*3 4] **Emmanouil Angelis** [*3 4] **Mathias Jacob Schreiner** [1] **Stefan Bauer** [3 4]
Andrea Dittadi [†3 4 5] **Simon Olsson** [†1]

Abstract

We propose a regularization framework inspired by thermodynamic work for guiding pre-trained probability flow generative models (e.g., continuous normalizing flows or diffusion models) by minimizing excess work, a concept rooted in statistical mechanics and with strong conceptual connections to optimal transport. Our approach enables efficient guidance in sparse-data regimes common to scientific applications, where only limited target samples or partial density constraints are available. We introduce two strategies: Path Guidance for sampling rare transition states by concentrating probability mass on user-defined subsets, and Observable Guidance for aligning generated distributions with experimental observables while preserving entropy. We demonstrate the framework's versatility on a coarse-grained protein model, guiding it to sample transition configurations between folded/unfolded states and correct systematic biases using experimental data. The method bridges thermodynamic principles with modern generative architectures, offering a principled, efficient, and physics-inspired alternative to standard fine-tuning in data-scarce domains. Empirical results highlight improved sample efficiency and bias reduction, underscoring its applicability to molecular simulations and beyond.

[*]Equal contribution [†]Joint last authors [1]Chalmers University of Technology and University of Gothenburg, Gothenburg, Sweden [2]Massachusetts Institute of Technology, Research Laboratory of Electronics, Cambridge, MA, USA [3]Technical University of Munich [4]Helmholtz AI, Munich [5]Max Planck Institute for Intelligent Systems, Tübingen. Correspondence to: Simon Olsson <simonols@chalmers.se>.

Proceedings of the Workshop on Generative AI for Biology at the 42nd International Conference on Machine Learning, Vancouver, Canada. PMLR 267, 2025. Copyright 2025 by the author(s).

1. Introduction

Probability flow generative models, such as normalizing flows (Papamakarios et al., 2021; Liu, 2022; Albergo et al., 2023; Lipman et al., 2023) and diffusion models (Song et al., 2020; Ho et al., 2020), enable the modeling of complex, high-dimensional data distributions across a wide range of applications. These models generate samples through the integration of differential equations evolving a tractable distribution into an approximation of the data distribution. Although these models excel at general distribution learning, many scientific applications require precise control over generated samples to meet sparse observational constraints (e.g., limited transition state configurations or partial density constraints from experiments). Current guidance methods struggle in data-scarce regimes as they typically rely on either specialized training or abundant reward signals.

Existing approaches often involve fine-tuning (Wallace et al., 2024; Black et al., 2023; Domingo-Enrich et al., 2024), incorporating conditional information during training (Ho & Salimans, 2022; Nichol et al., 2021), or training an additional noise-aware discriminative model (Song et al., 2020). While effective, these methods may be impractical in sparse-data settings. A prominent class of alternative approaches, known as *loss guidance*, perturbs the score of a frozen foundation model with guidance signals obtained via backpropagation through the model (Bansal et al., 2023; Chung et al., 2023; Song et al., 2023; Kawar et al., 2022) or through the full ODE (Ben-Hamu et al., 2024). Although successfully used for post hoc control, they can suffer from high gradient variance in high-dimensional, structured spaces, motivating the need for a more stable and principled regularization framework.

Inspired by statistical mechanics, we introduce an approach for regularizing guidance of probability flow generative models based on the principle of minimum excess work (MEW). In this context, "work" is a measure of the physical effort, e.g., energy, needed to transform a system from one macrostate to another, where a macrostate is characterized by a probability density function. MEW thereby acts as a natural, physics-inspired regularization scheme for guiding generative models. We develop the theoretical framework for MEW-based regularization of generative models, explicitly connecting it to optimal transport theory,

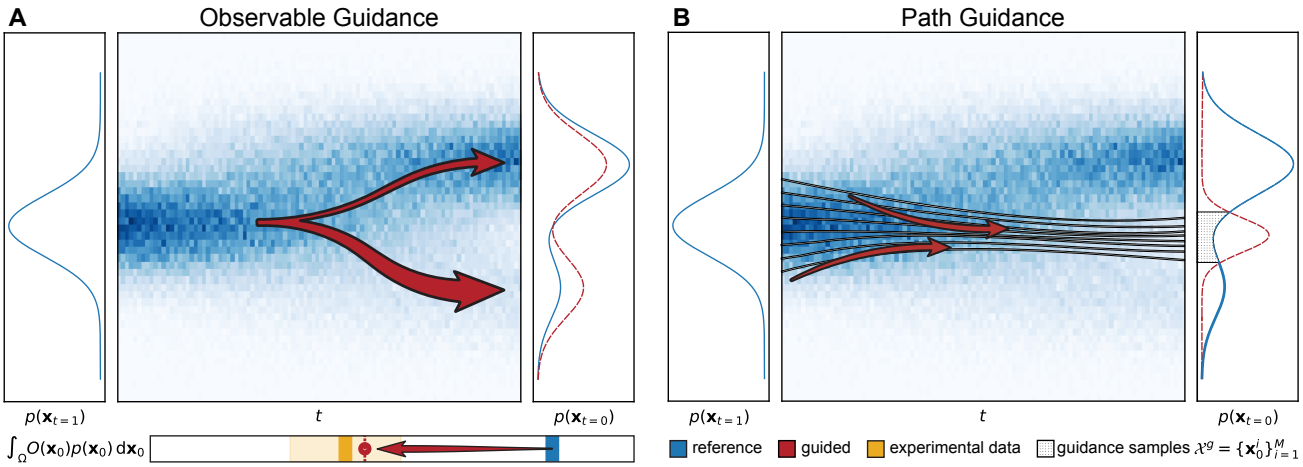

Figure 1: Schematic comparison of observable and path guidance. Both panels show the evolution of probability density over time t (blue heat map) with marginal distributions $p(\mathbf{x}_1)$ and $p(\mathbf{x}_0)$ on the sides (blue: reference model, red dashed: guided model). (A) Observable guidance perturbs the score function (red arrows) to match experimental observables (yellow) with unknown data distribution $p(\mathbf{x}_0)$ using minimal excess work. (B) Path guidance steers sampling trajectories (black solid) toward specific regions defined by guidance samples $\mathcal{X}^g = \{\mathbf{x}_0^i\}_{i=1}^M$ (dotted grey).

and validate its effectiveness through extensive benchmarks across multiple systems, including a coarse-grained protein Boltzmann Emulator. In addition to introducing the MEW framework, we propose a simple yet effective form of path guidance tailored to sparse sampling problems. We specialize MEW guidance to address two problems frequently encountered in molecular dynamics simulations. First, **Observable Guidance**: a bias correction method to align distributions with experimental observables while preserving distributional entropy. Second, **Transition State Sampling**: a path-guidance-based sampling strategy to focus sampling on a user-defined subset, e.g., the low-probability transition region between states.

2. Background and Preliminaries

Diffusion models learn a stochastic process that maps a simple prior distribution p_1 to an approximation p_0 of the data distribution q_0. This is typically done by reversing a known noising process governed by an Ornstein–Uhlenbeck SDE,

$$\mathrm{d}\mathbf{x}_t = \mathbf{f}(\mathbf{x}_t, t)\,\mathrm{d}t + g(t)\,\mathrm{d}\mathbf{w}_t \tag{1}$$

with $\mathbf{f}(\mathbf{x}_t, t)$ linear in $\mathbf{x}_t$. This process induces a family of marginals q_t with simple forward transitions $q_t(\mathbf{x}_t|\mathbf{x}_0) = \mathcal{N}(\mathbf{x}_t; \alpha_t\mathbf{x}_0, \sigma_t^2\mathbf{I})$, where α_t, σ_t are determined by the SDE coefficients. Given access to q_1 and the score $\nabla_{\mathbf{x}_t}\log q_t(\mathbf{x}_t)$, one can sample from q_0 via the time-reversal (Anderson, 1982):

$$\mathrm{d}\mathbf{x}_t = \left[\mathbf{f}(\mathbf{x}_t, t) - g(t)^2\nabla_{\mathbf{x}_t}\log q_t(\mathbf{x}_t)\right]\mathrm{d}t + g(t)\,\mathrm{d}\widetilde{\mathbf{w}}_t \tag{2}$$

where $\widetilde{\mathbf{w}}_t$ is a reverse-time Wiener process, or via the *probability flow ODE* (Maoutsa et al., 2020; Song et al., 2020):

$$\frac{\mathrm{d}\mathbf{x}_t}{\mathrm{d}t} = \mathbf{f}(\mathbf{x}_t, t) - \frac{1}{2}g(t)^2\nabla_{\mathbf{x}_t}\log q_t(\mathbf{x}_t) \tag{3}$$

both having the same time-marginals q_t as the forward process. In practice, the score is approximated by a score model $\mathbf{s}_\theta(\mathbf{x}_t, t)$, and a simple distribution $p_1 \approx q_1$ is used as initial distribution at $t = 1$:

$$\mathrm{d}\mathbf{x}_t = \left[\mathbf{f}(\mathbf{x}_t, t) - g(t)^2\mathbf{s}_\theta(\mathbf{x}_t, t)\right]\mathrm{d}t + g(t)\,\mathrm{d}\widetilde{\mathbf{w}}_t \tag{4}$$

$$\frac{\mathrm{d}\mathbf{x}_t}{\mathrm{d}t} = \mathbf{f}(\mathbf{x}_t, t) - \frac{1}{2}g(t)^2\mathbf{s}_\theta(\mathbf{x}_t, t) \tag{5}$$

We will denote by $\{p_t\}_{t\in[0,1]}$ the probability path induced by Equation (4) or Equation (5).

Equilibrium sampling of the Boltzmann distribution. A key challenge in statistical mechanics is to generate independent samples from the Boltzmann distribution

$$\mathbf{x} \sim p(\mathbf{x}) \propto \exp(-\beta U(\mathbf{x})), \tag{6}$$

where $\beta = (k_\mathrm{B}T)^{-1}$ is the inverse temperature and $U(\mathbf{x})$ is the potential energy of a configuration $\mathbf{x} \in \Omega \subseteq \mathbb{R}^d$. This distribution underlies estimation of macroscopic observables, such as $\mathbb{E}_{p(\mathbf{x})}[O_i(\mathbf{x})]$, which allow for a direct comparison to experimental data. However, sampling from $p(\mathbf{x})$ is notoriously difficult due to the rugged energy landscape $U(\mathbf{x})$. Traditional methods such as Molecular Dynamics (MD) or Markov Chain Monte Carlo (MCMC) suffer from slow mixing and generate highly correlated samples that often fail to cross energy barriers between metastable

states. This leads to biased estimates and poor coverage of transition configurations, i.e., regions in state space that are severely undersampled but mechanistically crucial. Recent work on Boltzmann Generators (Noé et al., 2019; Klein et al., 2024b; Midgley et al., 2023; Köhler et al., 2020; Moqvist et al., 2025; Tan et al., 2025) addresses these challenges by learning direct mappings from simple priors to Boltzmann-like distributions. Yet, two issues remain: inaccuracies in the potential energy model can bias the learned distribution (Kolloff et al., 2022; Klein et al., 2024a), and physically important but low-probability states (e.g., transition states) remain exponentially rare. In this work, we address both problems by guiding a generative model using sparse experimental or structural information, leveraging a coarse-grained Boltzmann emulator inspired by Arts et al. (2023).

Maximum Entropy Reweighting is a broadly adopted technique to overcome force field inaccuracies in potential energy models (Pitera & Chodera, 2012; Cavalli et al., 2013; Olsson et al., 2013; 2016; Boomsma et al., 2014; White & Voth, 2014; Beauchamp et al., 2014; Hummer & Köfinger, 2015; Bonomi et al., 2016). The result of this optimization is a tilted distribution which depends on a set of Lagrange multipliers, $\{\lambda_i\}$, each corresponding to an experimental observable of interest. The solution $p'(\mathbf{x}) \propto p(\mathbf{x}) \exp\big(-\sum_{i=1}^{M} \lambda_i O_i(\mathbf{x})\big)$ minimizes the KL divergence from the reference distribution $p(\mathbf{x})$, subject to the constraints $\mathbb{E}_{p'(\mathbf{x})}[O_i(\mathbf{x})] = o_i$. A detailed derivation is provided in Appendix A.1 for the reader's convenience. However, until now, this approach has been limited to reweighting fixed sets of samples $\mathcal{X} = \{\mathbf{x}_i\}_{i=1}^{M}$ (e.g., an MD trajectory), thus motivating methods to apply these principles in a generative setting.

Loss Guidance is the process of adjusting the diffusion process to satisfy a target condition $\mathbf{y}$ without fine-tuning and has been explored in several prior works (Bansal et al., 2023; Chung et al., 2023; Song et al., 2023). To sample from the conditional distribution $p(\mathbf{x}_0|\mathbf{y})$ *post hoc*, we can use the following identity: $\nabla_{\mathbf{x}_t} \log p(\mathbf{x}_t|\mathbf{y}) = \nabla_{\mathbf{x}_t} \log p(\mathbf{x}_t) + \nabla_{\mathbf{x}_t} \log p(\mathbf{y}|\mathbf{x}_t)$. Obtaining $\nabla_{\mathbf{x}_t} \log p(\mathbf{y}|\mathbf{x}_t)$ typically requires training a separate model on the noisy states $\mathbf{x}_t$, as done in classifier guidance (Song et al., 2020). Alternatively, the posterior mean $\hat{\mathbf{x}}_t(\mathbf{x}_t) := \mathbb{E}_{p(\mathbf{x}_0|\mathbf{x}_t)}[\mathbf{x}_0]$ can be used as an estimate of the clean data $\mathbf{x}_0$. Using Tweedie's formula, the posterior mean can be expressed as $\mathbb{E}_{p(\mathbf{x}_0|\mathbf{x}_t)}[\mathbf{x}_0] = \frac{1}{\alpha_t}(\mathbf{x}_t + \sigma_t^2 \nabla_{\mathbf{x}_t} \log p(\mathbf{x}_t))$. This allows us to approximate the likelihood in data space via $\log p(\mathbf{y}|\hat{\mathbf{x}}_t(\mathbf{x}_t)) \simeq \ell(\mathbf{y}, \hat{\mathbf{x}}_t(\mathbf{x}_t))$, where ℓ denotes a suitable differentiable loss function (e.g., cross-entropy or log-likelihood under a differentiable model). The gradient $\nabla_{\mathbf{x}_t} \log p(\mathbf{y}|\hat{\mathbf{x}}_t(\mathbf{x}_t))$ can then be computed by backpropagation. In practice, the mean is approximated using the score model $\mathbf{s}_\theta(\mathbf{x}_t, t)$, allowing the score estimate to be updated as $\nabla_{\mathbf{x}_t} \log p(\mathbf{x}_t|\mathbf{y}) \simeq \mathbf{s}_\theta(\mathbf{x}_t, t) + \eta_t \nabla_{\mathbf{x}_t} \ell(\hat{\mathbf{x}}_t(\mathbf{x}_t), \mathbf{y})$ with η_t being a guiding strength function.

Work and Optimal Transport. In statistical mechanics, thermodynamic work W is the energy required to transform a system from a probabilistic state p to another p'. For a continuum system:

$$W = \iint \mathbf{J}(\mathbf{x}, t) \cdot \mathbf{F}(\mathbf{x}, t) \, \mathrm{d}\mathbf{x} \, \mathrm{d}t, \tag{7}$$

where $\mathbf{J}(\mathbf{x}, t) = \mathbf{v}(\mathbf{x}, t) p_t(\mathbf{x})$ is the probability flux and $\mathbf{F}(\mathbf{x}, t)$ is the force applied to the system. This generalizes the classical work expression $W = \int F(\mathbf{x}) \, \mathrm{d}\mathbf{x}$. When the force and velocity field coincide (i.e., the Jacobian of the push-forward map associated with the velocity field is a diffeomorphism), they can be expressed as spatial gradients of a potential $u(\mathbf{x}, t)$ (Brenier, 1991). Under these conditions, W becomes equivalent to the kinetic energy in the Benamou–Brenier formulation of optimal transport (Benamou & Brenier, 2000), and provides an upper bound on the squared 2-Wasserstein distance between the distributions:

$$W_2^2(p, p') \leq \iint \|\mathbf{v}(\mathbf{x}, t)\|^2 p_t(\mathbf{x}) \, \mathrm{d}\mathbf{x} \, \mathrm{d}t = W \tag{8}$$

where $\mathbf{v}$ and p satisfy $\frac{\partial}{\partial t} p_t(\mathbf{x}) = -\nabla_{\mathbf{x}} \cdot [p_t(\mathbf{x}) \, \mathbf{v}(\mathbf{x}, t)]$. Minimizing W yields the optimal transport map that transforms p into p' along the path requiring minimal energy. The idea of identifying probability paths minimizing the kinetic energy, or more generally a Lagrangian, has recently been applied to improve the efficiency of probability flow generative models (Tong et al., 2020; 2023; Klein et al., 2023; Irwin et al., 2025; Shaul et al., 2023; Albergo et al., 2023; Neklyudov et al., 2023a;b).

3. Minimum-Excess-Work Guidance

During the generative process, we transform a simple distribution $p_1 \sim \mathcal{N}(\mathbf{0}, \mathbf{I})$ into a complex data distribution p_0 with support $\Omega \subseteq \mathbb{R}^d$ by solving the reverse-time SDE (4) or the ODE (5). To incorporate additional constraints and align the generative process with new information, we modify the drift in Equations (4) and (5) by augmenting the score model $\mathbf{s}_\theta(\mathbf{x}_t, t)$ with an additive correction $\mathbf{h}_\vartheta(\mathbf{x}_t, t)$, resulting in $\mathbf{r}_{\theta,\varphi}(\mathbf{x}_t, t) = \mathbf{s}_\theta(\mathbf{x}_t, t) + \mathbf{h}_\vartheta(\mathbf{x}_t, t)$, such that :

$$\mathrm{d}\mathbf{x}_t = \big[\mathbf{f}(\mathbf{x}_t, t) \, \mathrm{d}t - g(t)^2 \mathbf{r}_{\theta,\varphi}(\mathbf{x}_t, t)\big] \, \mathrm{d}t + g(t) \, \mathrm{d}\widetilde{\mathbf{w}}_t \tag{9}$$

$$\frac{\mathrm{d}\mathbf{x}_t}{\mathrm{d}t} = \mathbf{f}(\mathbf{x}_t, t) - \frac{1}{2} g(t)^2 \mathbf{r}_{\theta,\varphi}(\mathbf{x}_t, t) \tag{10}$$

where $\mathbf{h}_\vartheta : \mathbb{R}^d \times [0, 1] \to \mathbb{R}^d$ is a time-dependent vector field.

The aim of MEW guidance is to satisfy a guidance objective for the guided distribution $p_0' \neq p_0$, while minimizing

the *excess work* associated with $\mathbf{h}_\vartheta(\mathbf{x}_t, t)$, required to modify the probability density, p_0.

We define the excess work in the context of an unperturbed and perturbed system described by the following ODEs over $t \in [0, 1]$:

$$\frac{\mathrm{d}\mathbf{x}_t}{\mathrm{d}t} = \mathbf{v}(\mathbf{x}_t, t)\,, \qquad \frac{\mathrm{d}\mathbf{x}_t}{\mathrm{d}t} = \mathbf{v}(\mathbf{x}_t, t) + \mathbf{u}(\mathbf{x}_t, t)\,, \quad (11)$$

with the respective time-marginal densities p_t, p'_t, where we assume $p_1 = p'_1$.

Loosely following Equation (8), we define the excess work as $\Delta W := \iint \|\mathbf{u}(\mathbf{x}, t)\|^2 \, p'_t(\mathbf{x}) \, \mathrm{d}\mathbf{x} \, \mathrm{d}t$, which for the ODEs (5) and (10) becomes:

$$\Delta W(\vartheta) = \iint \frac{g(t)^4}{4} \|\mathbf{h}_\vartheta(\mathbf{x}, t)\|^2 \, p'_t(\mathbf{x}) \, \mathrm{d}\mathbf{x} \, \mathrm{d}t\,. \quad (12)$$

We will now establish quantitative relationships between the perturbation of the model and the changes it induces in the generated distribution. Detailed proofs are provided in Appendices A.2 and A.3.

Proposition 3.1. *Let p_t and p'_t be the distributions at time t obtained by solving the ODEs (5) and (10) backwards in time from the same initial distribution p_1 at $t = 1$. Assume that the vector fields are measurable in time and L_t-Lipschitz in space with L_t integrable. Then:*

$$W_2^2(p_0, p'_0) \leq \int_0^1 w_{\mathrm{W}}(t) \, \frac{g(t)^4}{4} \, \mathbb{E}_{\mathbf{x}\sim p'_t} \left[\|\mathbf{h}_\vartheta(\mathbf{x}, t)\|^2 \right] \mathrm{d}t, \quad (13)$$

with $w_{\mathrm{W}}(t) := e^{t + 2\int_0^t L_s \, \mathrm{d}s}$

Proposition 3.2. *Let p_t and p'_t be the distributions at time t induced by the reverse-time SDEs (4) and (9) starting from the same distribution p_1 at $t = 1$. Assume that both SDEs admit strong solutions, and that $\mathbb{P}' \ll \mathbb{P}$, where $\mathbb{P}, \mathbb{P}'$ are the path measures induced by the SDEs on $C([0, 1], \mathbb{R}^d)$. Then:*

$$D_{\mathrm{KL}}(p'_0 \| p_0) \leq \int_0^1 w_{\mathrm{KL}}(t) \, \frac{g(t)^4}{4} \, \mathbb{E}_{\mathbf{x}\sim p'_t} \left[\|\mathbf{h}_\vartheta(\mathbf{x}, t)\|^2 \right] \mathrm{d}t, \quad (14)$$

with $w_{\mathrm{KL}}(t) := \frac{2}{g(t)^2}$

Since both bounds—for the KL divergence and the Wasserstein distance—are time-reweighted versions of the excess work ΔW (12), it serves as a natural choice of regularizer for guidance objectives, encouraging the perturbed distribution p'_0 to remain close to the reference base distribution p_0.

We then optimize the parameters ϑ of the perturbation $\mathbf{h}_\vartheta$ by minimizing the following objective:

$$\mathcal{L}(\vartheta) = \mathcal{L}_1(\vartheta) + \gamma \, \Delta W(\vartheta)\,, \quad (15)$$

where $\mathcal{L}_1(\vartheta)$ is a guidance objective, and γ controls the regularization strength.

We now explore how this minimum-excess-work principle is applied in the two settings: (1) guidance based on expectations of observables; (2) targeted guidance towards a user-defined subspace.

Observable Guidance. In this section, we guide a diffusion model to align with data that reflects an expectation, using the MEW approach. Using a set of Lagrange multipliers $\Lambda = \{\lambda_1, ..., \lambda_M\}$ pre-estimated using, e.g., the algorithm outlined in Bottaro et al. (2020), we dynamically adjust the score by estimating an augmentation factor $\mathbf{h}_\vartheta$ that ensures $\left|\mathbb{E}_{p'(\mathbf{x})}[O_i(\mathbf{x})] - o_i\right| \leq \epsilon$. We express the guidance factor as,

$$\mathbf{h}_\vartheta(\mathbf{x}_t, t) = -\eta_t(\vartheta) \sum_{i=1}^{M} \lambda_i \nabla_{\mathbf{x}_t} O_i(\hat{\mathbf{x}}_t(\mathbf{x}_t))\,. \quad (16)$$

In the same way that a score model $\mathbf{s}_\theta(\mathbf{x}_t, t)$ approximates the gradient of the log probability, $\mathbf{h}_\vartheta(\mathbf{x}_t, t)$ is the gradient of the observable function with respect to the latent variable $\mathbf{x}_t$. λ_i steers the flow in directions favored (or penalized) by the experimental observable expectation, thus "adjusting" the score of the original model. Its amplitude is modulated by $\eta_t(\vartheta) = \eta_{\text{init}} \exp(-\kappa(1 - t))$, and learning the parameters $\vartheta = \{\eta_{\text{init}}, \kappa\}$ of this scalar function constitutes the primary objective of our optimization strategy. Note, we use the mean posterior estimation $\hat{\mathbf{x}}_t(\mathbf{x}_t)$ discussed in Section 2, instead of using $\mathbf{x}_t$ directly (Bansal et al., 2023; Chung et al., 2023). Our optimization objective is two-fold: We want to reduce the discrepancies between the model predictions and experimental data while minimizing the excess work exerted by the augmentation. The former is a supervised loss defined as

$$\mathcal{L}_1(\vartheta) = \frac{1}{M} \sum_{i=1}^{M} \left(o_i^{\text{exp}} - \mathbb{E}_{\mathbf{x}\sim p'_0}[O_i(\mathbf{x})] \right)^2, \quad (17)$$

where o_i^{exp} are the experimental values and $\mathbb{E}_{\mathbf{x}\sim p'_0}[O_i(\mathbf{x})]$ denotes the expected values under the adjusted distribution p'_0. To balance accuracy with the principle of maximum entropy, we introduce a regularization term based on minimizing the excess work ΔW. Substituting the specific form of $\mathbf{h}_\vartheta(\mathbf{x}_t, t)$ from Equation (16) into Equation (12), we obtain:

$$\Delta W(\vartheta) = \int_0^1 \frac{g(t)^4}{4} |\eta_t(\vartheta)|^2 \cdot \mathbb{E}_{\mathbf{x}\sim p'_t} \left[\left\| \sum_{i=1}^{M} \lambda_i \nabla_{\mathbf{x}} O_i(\hat{\mathbf{x}}_t(\mathbf{x})) \right\|^2 \right] \mathrm{d}t\,. \quad (18)$$

Path Guidance. In this setting, we assume access to a set of guiding samples $\mathcal{X}^g = \{\mathbf{x}^i\}_{i=1}^M$, each belonging to a target

subset $A \subset \Omega$ of the sampling space. The goal is to modify the score of the diffusion model to sample from a perturbed distribution $\mathbf{x} \sim p_0'$ that increases the likelihood of $\mathbf{x} \in A$. Since $\mathcal{L}_1$ need not be differentiable, the objective can be formulated generally as:

$$\mathcal{L}_1(\vartheta, \varphi) = 1 - \frac{1}{N}\mathbb{E}_{\mathbf{x}\sim p_0'}\left[\mathbb{1}_{\{\mathbf{x}\in A\}}\right] . \tag{19}$$

Guiding the diffusion process towards the subset A can be done by taking advantage of the probability flow ODE (5), which holds the desirable property of providing unique *latent representations* of each data point, for any time step t. Starting from the guiding samples, we compute their trajectories by integrating Equation (5) forward in time, obtaining the latent representations $\mathcal{X}_t^g = \{\mathbf{x}_t^i\}_{i=1}^M$ for time t. The set $\{\mathcal{X}_t^g\}_{t=0}^1$ defines a trajectory of latent representations that the model must follow to ensure its samples satisfy $\mathbf{x}' \in A$. Based on this trajectory, we can define the augmentation factor as:

$$\mathbf{h}_{\vartheta,\varphi}(\mathbf{x}_t, t) \coloneqq \eta_t(\vartheta)\nabla_{\mathbf{x}_t} \log \mathcal{K}_{h_t(\varphi)}(\mathbf{x}_t, \mathcal{X}_t^g) \tag{20}$$

with $\mathcal{K}_{h_t(\varphi)}(\mathbf{x}_t, \mathcal{X}_t^g) \coloneqq \sum_{\mathbf{x}_t^i \in \mathcal{X}_t^g} \mathrm{K}_{h_t(\varphi)}(\mathbf{x}_t, \mathbf{x}_t^i)$ where K can be any differentiable kernel with time-dependent bandwidth $h_t(\varphi)$. By updating the score function using Equation (20), we align the sampling trajectory with that of the guiding points, while regularizing the guidance strength via the same excess work penalty as in Equation (18), now evaluated using the time-dependent KDE score $\mathbb{E}_{\mathbf{x}\sim p_t'}\left[\|\nabla_{\mathbf{x}} \log \mathcal{K}_{h_t(\varphi)}(\mathbf{x}, \mathcal{X}_t^g)\|\right]$. In practice, both $\eta_t(\vartheta)$ and $h_t(\varphi)$ are implemented as sigmoid functions

$$\eta_t(\vartheta) = \vartheta_{init}\left(1 - \sigma(\vartheta_g(t - \vartheta_s))\right) \tag{21}$$

$$h_t(\varphi) = \varphi_{init} + \sigma(\varphi_g(t - \varphi_s)) \tag{22}$$

with learnable parameters $\vartheta = (\vartheta_{init}, \vartheta_g, \vartheta_s)$ and $\varphi = (\varphi_{init}, \varphi_g, \varphi_s)$ and optimized for Equation (15) using Bayesian optimization with Gaussian Processes. The use of sigmoids allows the guidance to be stronger early in the trajectory, when $\mathbf{x}_t$ is close to the Gaussian prior and the kernel signal is more stable, and weaker near $t = 0$, where the data distribution is more complex and direct guidance is less reliable.

4. Experiments

We now demonstrate the application of minimum-excess-work guidance across several experimental setups. We first evaluate path and observable guidance on two toy setups and will then proceed to showcase our approach on a coarse-grained protein Boltzmann Emulator.

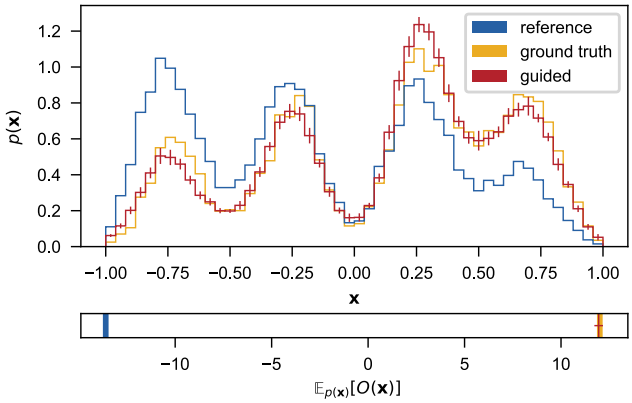

Figure 2: **Comparison of Probability Distributions Before and After Observable Guidance for a 1D Energy Potential.** The top plot shows the probability distributions for three models: the biased reference model (blue), the ground truth model (yellow), and the guided model (red). Guidance helps to align the reference model with that of the ground truth model using only the expectation of an observable function (bottom) while minimizing excess work.

4.1. Observable Guidance

4.1.1. Synthetic Data

To evaluate our approach, we target a synthetic dataset where the ground truth is available. We trained a diffusion model on samples from a biased 1D quadruple-well potential (Prinz et al., 2011), a simple test system displaying two key properties in molecular dynamics: multi-modality and metastability, while keeping the corresponding Boltzmann distribution is numerically accessible, allowing us to directly gauge our methods' ability to recover the unbiased distribution.

Experimental Setup. The observable function is implemented as a Gaussian mixture model with four components. We compute the Lagrange multiplier following (Bottaro et al., 2020) and integrate it into our guidance framework via Equation (9). The model is evaluated by comparing the expectation values of the observable function and the KL divergence from the ground truth. The experimental details can be found in Appendix B.3.

Evaluation. Figure 2 shows the sampled probability distributions and observable values for three models: the biased reference model (blue), ground truth (GT) (yellow), and our guided model (red). The guided model successfully recovers the GT using only the observable expectation value as supervision. Quantitatively, Table 1 shows our method reduces the KL divergence by a factor of 10 from 0.13 to 0.019 ± 0.002 and brings the observable expectation from -13.6 to 11.95 ± 0.22, nearly matching the GT of 12.01.

Ablation. To evaluate the impact of MEW regularization, we performed an ablation study comparing the observable-guided model trained with ($\gamma > 0$) and without ($\gamma = 0$) MEW. As shown in Table 4 and visualized in Figure 9 (in the

Table 1: Metrics for $O(\mathbf{x})$ and KL divergence across models.

Model $\mathcal{M}$	$\mathbb{E}_{p_{\mathcal{M}}(\mathbf{x})}[O(\mathbf{x})]$	$\mathrm{KL}[p_{\mathrm{GT}}(\mathbf{x})\|p_{\mathcal{M}}(\mathbf{x})]$
Ground Truth	12.01	—
Reference	-13.6	0.13
Guided	11.95 ± 0.22	0.019 ± 0.002

Appendix), both models generate similar expected observables. However, the model trained without MEW suffers from mode collapse, concentrating all probability density in a narrow region of state space and exhibiting poor distributional fidelity. In contrast, MEW-regularized training preserved the broader shape of the reference distribution. This results highlights the impact of MEW regularization by stabilizing training and preventing degenerate solutions.

This synthetic experiment demonstrates empirically that our method enables guiding of a biased model toward the correct distribution using only expectation values, while maintaining similarity to the reference through MEW regularization.

4.1.2. Coarse-Grained Protein Boltzmann Emulator (cgBE)

To evaluate our method on a real-world task, we apply observable guidance to guide a pre-trained cgBE to sample conformations of chignolin, a ten-residue mini-protein that serves as a standard benchmark in protein folding studies (Honda et al., 2004; Satoh et al., 2006; Lindorff-Larsen et al., 2011). Our task is to correct systematic biases in the equilibrium sampling using only experimental measurements while preserving physical validity. This is a challenging task given the high-dimensional structured space and unknown ground truth distribution.

Experimental Setup. We use folding free energy $\Delta G = -k_B T \log(\frac{p_{\text{folded}}}{p_{\text{unfolded}}})$ as our observable, which captures the relative stability of different protein conformations. The reference model p_{MD} shows significant bias in this metric (-1.27 kcal/mol vs. experimental value of -1.87 kcal/mol (Honda et al., 2004)), making it a suitable test case. Model architecture and training details are provided in Appendix B.3.

Evaluation. Our guided model achieves substantial improvements across several metrics (see Table 2) while maintaining physical validity, which we verified through the analysis of bond lengths and torsion angles (Figures 6 to 8, in the Appendix). The guided model's folding free energy (-1.82 ± 0.01 kcal/mol) closely matches the target experimental value (-1.87 kcal/mol), reducing mean squared error by an order of magnitude from 0.6 to 0.05 kcal/mol. Additionally, the KL divergence from the reference MD trajectory improves from 0.329 to 0.005 ± 0.002, demonstrating better conservation of the properties of the reference distribution, including multi-modality and entropy. Figure 3

Table 2: Quantitative metrics evaluating the guidance process: expected observables and KL divergence across models.

Model $\mathcal{M}$	$\mathbb{E}_{p_{\mathcal{M}}(\mathbf{x})}[O(\mathbf{x})]$ (kcal/mol)	$\mathrm{KL}[p'_{\mathrm{MD}}(\mathbf{x})\|p_{\mathcal{M}}(\mathbf{x})]$
Experimental	-1.87	—
Reference	-1.27	0.329
Guided	-1.82 ± 0.01	0.005 ± 0.002

visualizes these improvements. Panels A and B demonstrate that guidance successfully increases the population of folded states, consistent with experimental observations. Panel C shows 50 superimposed generated structures, highlighting both the diversity and physical validity of our samples.

These results demonstrate that guidance in the sparse-data regime with MEW regularization allows allows us to effectively align high-dimensional and highly structured generative models with experimental constraints without compromising local physical validity and maintaining global distributional properties such as multi-modality.

4.2. Path Guidance

We now use the cgBE to evaluate path guidance with MEW regularization for up-sampling high-energy transition configurations (states), which are critical for understanding the folding process of proteins. Due to their high energy (Equation (6)), these states account for only 1% of both the data and model distribution, making their successful up-sampling a strong demonstration of our method's effectiveness. Consistent with Section 4.1, we also use the chignolin mini-protein as a test system. To contextualize path guidance, we first introduce an alternative baseline.

Baseline. As a natural alternative to path guidance, we adapt loss guidance to our setting by using the log-likelihood of a KDE fitted on guiding points $\mathcal{X}_0^g = \{\mathbf{x}_0^i\}_{i=1}^M$. Specifically, we will change the perturbation Kernel from Equation (20) to $\mathcal{K}_{h_t(\varphi)}(\hat{\mathbf{x}}_t(\mathbf{x}_t), \mathcal{X}_0^g)$. While it appears similar to path guidance, the key difference lies in the space the KDE is computed. In path guidance, the kernel is applied along the trajectory $\{\mathcal{X}_t^g\}_{t=0}^{t=1}$, resulting in a distinct KDE for each time step t. In contrast, loss guidance computes the KDE in data space and estimates the likelihood with respect to the posterior mean $\hat{\mathbf{x}}_t(\mathbf{x}_t)$, which requires backpropagating through the model at every sampling step. Implementation details and ablation studies for two alternative baselines that do not augment the vector field are provided in Appendix B.4 and Appendix D.3.

Evaluation Criteria. We assess the methods using three key metrics. First, we measure guiding success as the percentage of sampled transition configurations (see Appendix B.2 for details). Second, we evaluate the diversity among transition states using the Vendi score (VS) (Friedman & Dieng, 2022)

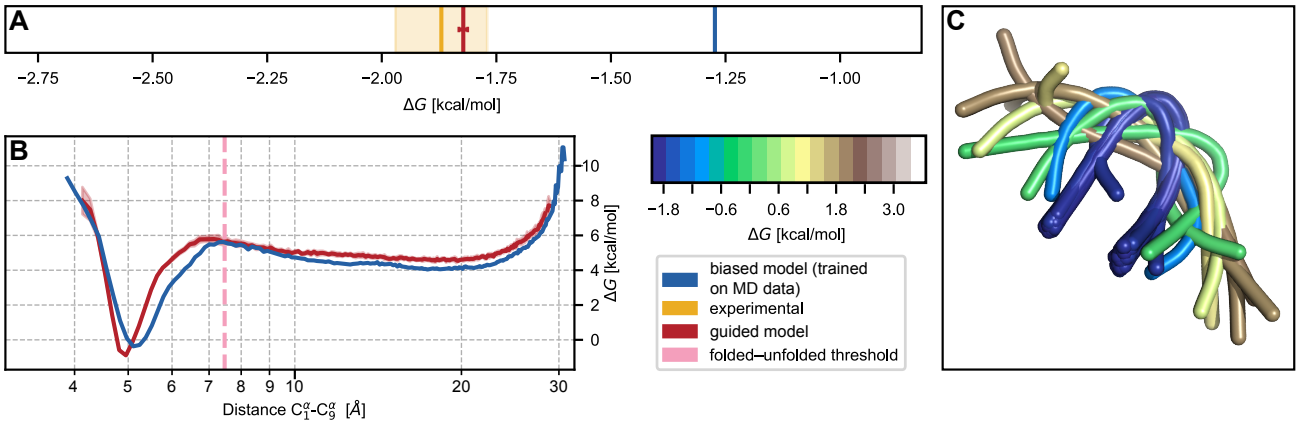

Figure 3: **Observable Guidance of a Protein Folding Model.** (A) Folding free energy comparison between reference model (blue), experimental data (yellow), and guided model (red). (B) Free energy profiles as a function of N- to C-terminal C^α distance. (C) Ensemble of 50 generated protein structures colored by their energy.

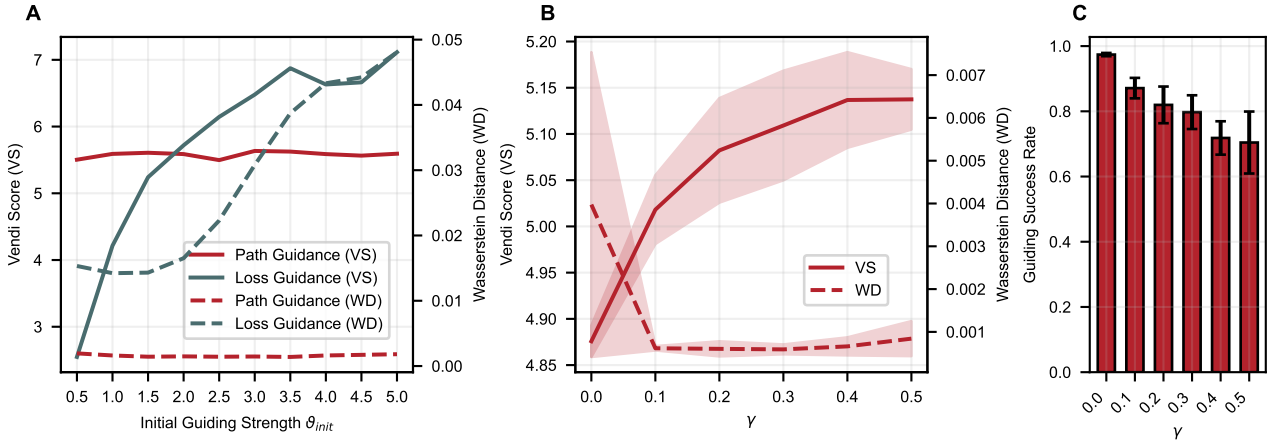

Figure 4: **Path Guidance vs. Loss-Guidance for sampling Transition States**. (A) Sample quality and diversity, measured by the Wasserstein Distance (WD) and Vendi score (VS), show that path guidance preserves diversity and quality even at high guiding strengths, whereas loss guidance deteriorates. (B) Without MEW regularization ($\gamma = 0$), the sampled transition states collapse and exhibit little to no diversity (VS). Regularization also improves sample quality (WD). (C) Guiding success rate, measured as the percentage of transition states sampled, for different regularization strengths.

to verify that our method generates novel samples rather than merely resampling the guiding data. Lastly, since we cannot evaluate the energy under the coarse-grained model, we instead ensure physical validity of the generated samples under guidance by computing the Wasserstein distance (WD) between the bond length distributions of generated and ground truth samples, which quantifies how well our method preserves the local molecular structure.

Synthetic Experiments. To explore the dynamics of both methods, we design a synthetic example (see Appendix D.1 for details). While ODE sampling offers better control, it often produces degenerate samples, as the guiding term $\mathbf{h}_{\vartheta,\varphi}(\mathbf{x}_t, t)$ can push trajectories off the data manifold, an issue SDE sampling can correct for through noise injection. As a result, SDE sampling proves more robust, maintaining sample diversity and quality while achieving comparable guidance success. Based on these findings, we use SDE sampling for all subsequent experiments. Additionally, we tested various guiding strength $\eta_t(\vartheta)$ and KDE bandwidth $h_t(\varphi)$ functions, finding step-like sigmoid functions both effective and easy to optimize.

Transition State Sampling. For the transition configuration sampling task, we adapt the kernel to handle rigid-body transformations using the Kabsch algorithm (Kabsch, 1976) akin to that adopted in (Pasarkar et al., 2023). Since we found loss guidance to be difficult to optimize in this application, we first performed a large grid search to identify optimal parameters for a fair comparison. This analysis revealed that increasing the guidance strength deteriorates sample quality in loss guidance, preventing it from achieving meaningful guiding success (Figure 12B). The performance gap stems from two key disadvantages of loss guidance, both

linked to the fact that the KDE is fitted in data space. First, loss guidance requires using the mean of the posterior to compute the augmentation factor, which, especially at early time steps t, suffers from very high variance. Second, at later time steps, while the predictions become more accurate, the KDE fails to capture the actual distribution of the guiding points effectively, as it is not well-suited for high data complexity. As a result, the loss signal can degrade the sampled data, which is evident from the increasing Wasserstein distance as the guiding strength ϑ_{init} increases (Figure 4A). In contrast, path guidance circumvents this issue by applying stronger guidance at higher time steps, where the latent is primarily noise, and decreasing the guiding strength over time. Notably, in Figure 4A, we observe that both the quality and diversity remain largely unaffected by the initial guiding strength ϑ_{init}. We further investigate the difference between path and loss guidance in Appendix D.2.

After observing that loss guidance could not be reliably optimized, we conducted a separate set of experiments to evaluate path guidance within the MEW framework by optimizing the objective in Equation (15). Disabling regularization ($\gamma = 0$) results in the highest guidance success rates (Figure 4C), but produces highly degenerate samples and reduced structural diversity, as indicated by the large variance in Wasserstein distance. In contrast, applying MEW regularization improves both sample quality and diversity (Figure 4B), while incurring only a modest reduction in guidance success. Overall, our results demonstrate that path guidance offers a strong alternative to loss guidance, and that MEW regularization is essential for robust and physically meaningful sampling in data-sparse regimes.

5. Related Works

Guidance of diffusion models. Guiding diffusion models during inference has been extensively explored. While earlier methods relied on training classifiers on noisy states (Song et al., 2020) or conditioning models during training (Ho & Salimans, 2022; Nichol et al., 2021), recent approaches guide inference without extra training, using the pre-trained model as a prior and incorporating loss-based signals (Bansal et al., 2023; Chung et al., 2023; Song et al., 2023; Kawar et al., 2022; Ben-Hamu et al., 2024). Our method follows this line, but introduces a regularization framework inspired by thermodynamic principles.

Stochastic Optimal Control. MEW also naturally connects to recent advances in stochastic optimal control (SOC) applied to diffusion and flow-based generative models. In particular, to approaches which consider steering generative trajectories by balancing a task-specific objective, such as aligning with experimental observables or reward models with a regularization that penalizes deviation from a pre-trained base model. In those works (Uehara et al., 2024; Domingo-Enrich et al., 2024; Han et al., 2024; Tang, 2024), fine-tuning the diffusion model is framed as a SOC problem that minimizes control effort while achieving alignment with downstream goals. Conceptually, the Minimum Excess Work principle plays an analogous role to the control cost in SOC, regularizing path perturbations to preserve the prior's structure while achieving target objectives. This connection situates the MEW framework within the broader trend of leveraging control-theoretic principles, including KL and f-divergence regularization, to derive principled, sample-efficient, and robust fine-tuning strategies for probabilistic generative models.

Transition ensemble sampling. Traditional methods like transition path sampling (Bolhuis et al., 2000; Cabriolu et al., 2017) use Monte Carlo in trajectory space, while recent machine learning approaches (Liu et al., 2025) employ neural networks but require extensive training data or predefined collective variables. Instead of explicit path sampling, we guide the generative process using latent representations of known transition states. While related to recent work using Boltzmann Generators (Plainer et al., 2023), our approach directly modifies the score function during sampling rather than performing MCMC moves between paths, enabling more efficient exploration of transition regions.

Reweighting with experimental data. Reweighting molecular dynamics simulations using experimental data has a long history in computational chemistry and biophysics. Theoretical work (Roux & Weare, 2013; Cavalli et al., 2013; Boomsma et al., 2014; Pitera & Chodera, 2012) adopted Jaynes (1957) Maximum Entropy approach to the problem, following several early experimental studies (Lindorff-Larsen et al., 2005; Dedmon et al., 2004; Cesari et al., 2018) based on replica-averaged simulations, giving a theoretical foundation for these approaches. This work was later complemented by probabilistic and Bayesian perspectives (Olsson et al., 2013; Bottaro et al., 2020; Bonomi et al., 2016; 2018), some of which specifically focused on reweighing (Hummer & Köfinger, 2015; Olsson et al., 2016; 2017; Kolloff & Olsson, 2023).

6. Limitations

Despite the strong empirical performance of MEW guidance across diverse settings, several limitations merit consideration. These primarily stem from the assumptions underpinning the method's application—for instance, that physical observables or representative samples can be leveraged to correct expectation values or guide sampling in low-density regions. While these assumptions do not demand perfect model accuracy, they do require that the model be sufficiently expressive and responsive to the applied guidance. If key modes are absent, convergence to meaningful distributions may be compromised. Additionally, the current

framework assumes differentiable observables and guidance targets, restricting its applicability in discrete or non-differentiable domains. Lastly, although scalability has been demonstrated in moderate settings, further evaluation is necessary for high-dimensional problems and large-scale simulators.

7. Conclusion

In this work, we introduced minimum-excess-work (MEW) guidance, a physics-inspired framework for regularizing the guidance of pre-trained probability flow generative models by regularizing *excess work*. Our analysis shows that this thermodynamically motivated regularization is closely connected to upper bounds on the Wasserstein distance and the KL divergence between the reference and guided distributions. We demonstrated the effectiveness of MEW regularization in two settings: *Observable Guidance* and *Path Guidance*. These approaches enable alignment with sparse experimental constraints and targeted sampling in low-density regions, while maintaining model flexibility. By penalizing excess work, our method reduces bias and enhances the sampling of rare, physically meaningful configurations, without degrading sample quality. Our results position MEW guidance as a principled and effective tool for bias correction and informed exploration in data-scarce scientific applications.

Impact Statement

This paper presents work whose goal is to advance the field of Machine Learning. There are many potential societal consequences of our work, none which we feel must be specifically highlighted here.

Acknowledgments and Disclosure of Funding

This work was partially supported by the Wallenberg AI, Autonomous Systems and Software Program (WASP) funded by the Knut and Alice Wallenberg Foundation, the Helmholtz Foundation Model Initiative, and the Helmholtz Association. The authors gratefully acknowledge the Gauss Centre for Supercomputing e.V. (www.gauss-centre.eu) for funding this project by providing computing time through the John von Neumann Institute for Computing (NIC) on the GCS Supercomputer JUPITER | JUWELS (Jülich Supercomputing Centre, 2021) at Jülich Supercomputing Centre (JSC). Preliminary results were enabled by resources provided by the National Academic Infrastructure for Supercomputing in Sweden (NAISS) at Alvis (project: NAISS 2023/22-1289), partially funded by the Swedish Research Council through grant agreement no. 2022-06725. The authors also acknowledge the MIT Office of Research Computing and Data for providing high-performance computing resources that have contributed to the research results reported within this paper. TH and AD acknowledge support from G-Research.

References

Albergo, M. S., Boffi, N. M., and Vanden-Eijnden, E. Stochastic interpolants: A unifying framework for flows and diffusions. *arXiv preprint arXiv:2303.08797*, 2023.

Anderson, B. D. Reverse-time diffusion equation models. *Stochastic Processes and their Applications*, 12(3):313–326, 1982.

Arts, M., Satorras, V. G., Huang, C.-W., Zuegner, D., Federici, M., Clementi, C., Noé, F., Pinsler, R., and van den Berg, R. Two for one: Diffusion models and force fields for coarse-grained molecular dynamics. *arXiv*, 2023.

Bansal, A., Chu, H.-M., Schwarzschild, A., Sengupta, S., Goldblum, M., Geiping, J., and Goldstein, T. Universal guidance for diffusion models. In *Proceedings of the IEEE/CVF Conference on Computer Vision and Pattern Recognition*, pp. 843–852, 2023.

Beauchamp, K. A., Pande, V. S., and Das, R. Bayesian energy landscape tilting: towards concordant models of molecular ensembles. *Biophysical journal*, 106(6):1381–1390, 2014.

Ben-Hamu, H., Puny, O., Gat, I., Karrer, B., Singer, U., and Lipman, Y. D-flow: Differentiating through flows for controlled generation. *arXiv preprint arXiv:2402.14017*, 2024.

Benamou, J.-D. and Brenier, Y. A computational fluid mechanics solution to the monge-kantorovich mass transfer problem. *Numerische Mathematik*, 84(3):375–393, 2000.

Black, K., Janner, M., Du, Y., Kostrikov, I., and Levine, S. Training diffusion models with reinforcement learning. *arXiv preprint arXiv:2305.13301*, 2023.

Bolhuis, P. G., Dellago, C., Geissler, P. L., and Chandler, D. Transition path sampling: throwing ropes over mountains in the dark in the uk transition path sampling: throwing ropes over mountains in the dark. *J. Phys.: Condens. Matter*, 12, 2000.

Bonomi, M., Camilloni, C., Cavalli, A., and Vendruscolo, M. Metainference: A bayesian inference method for heterogeneous systems. *Science advances*, 2(1):e1501177, 2016.

Bonomi, M., Pellarin, R., and Vendruscolo, M. Simultaneous determination of protein structure and dynamics using cryo-electron microscopy. *Biophysical journal*, 114 (7):1604–1613, 2018.

Boomsma, W., Ferkinghoff-Borg, J., and Lindorff-Larsen, K. Combining experiments and simulations using the maximum entropy principle. *PLoS computational biology*, 10(2):e1003406, 2014.

Bottaro, S., Bengtsen, T., and Lindorff-Larsen, K. Integrating molecular simulation and experimental data: a bayesian/maximum entropy reweighting approach. *Structural bioinformatics: methods and protocols*, pp. 219–240, 2020.

Bowman, G. R., Beauchamp, K. A., Boxer, G., and Pande, V. S. Progress and challenges in the automated construction of Markov state models for full protein systems. *Journal of Chemical Physics*, 131(12), 2009. ISSN 00219606. doi: 10.1063/1.3216567.

Bowman, G. R., Pande, V. S., and Noe, F. *An Introduction to Markov State Models and Their Application to Long Timescale Molecular Simulation (Advances in Experimental Medicine and Biology*. Springer Science+Business Media Dordrecht, volume 797 edition, 2014. ISBN 9789400776050.

Brenier, Y. Polar factorization and monotone rearrangement of vector-valued functions. *Communications on pure and applied mathematics*, 44(4):375–417, 1991.

Bressan, A. and Piccoli, B. *Introduction to the mathematical theory of control*, volume 1. American institute of mathematical sciences Springfield, 2007.

Cabriolu, R., Skjelbred Refsnes, K. M., Bolhuis, P. G., and van Erp, T. S. Foundations and latest advances in replica exchange transition interface sampling. *The Journal of Chemical Physics*, 147(15), 2017.

Cavalli, A., Camilloni, C., and Vendruscolo, M. Molecular dynamics simulations with replica-averaged structural restraints generate structural ensembles according to the maximum entropy principle. *The Journal of chemical physics*, 138(9), 2013.

Cesari, A., Reißer, S., and Bussi, G. Using the maximum entropy principle to combine simulations and solution experiments. *Computation*, 6(1):15, February 2018. ISSN 2079-3197.

Chung, H., Kim, J., Mccann, M. T., Klasky, M. L., and Ye, J. C. Diffusion posterior sampling for general noisy inverse problems. In *The Eleventh International Conference on Learning Representations*, 2023.

Dedmon, M. M., Lindorff-Larsen, K., Christodoulou, J., Vendruscolo, M., and Dobson, C. M. Mapping long-range interactions in α-synuclein using spin-label nmr and ensemble molecular dynamics simulations. *Journal of the American Chemical Society*, 127(2):476–477, December 2004. ISSN 1520-5126.

Domingo-Enrich, C., Drozdzal, M., Karrer, B., and Chen, R. T. Adjoint matching: Fine-tuning flow and diffusion generative models with memoryless stochastic optimal control. *arXiv preprint arXiv:2409.08861*, 2024.

E., W. and Vanden-Eijnden, E. Towards a theory of transition paths. *Journal of Statistical Physics*, 123(3): 503–523, May 2006. ISSN 1572-9613. doi: 10.1007/s10955-005-9003-9. URL http://dx.doi.org/10.1007/s10955-005-9003-9.

Friedman, D. and Dieng, A. B. The vendi score: A diversity evaluation metric for machine learning. *arXiv preprint arXiv:2210.02410*, 2022.

Han, Y., Razaviyayn, M., and Xu, R. Stochastic control for fine-tuning diffusion models: Optimality, regularity, and convergence. *arXiv preprint arXiv:2412.18164*, 2024.

Head, T., Kumar, M., Nahrstaedt, H., Louppe, G., and Shcherbatyi, I. scikit-optimize/scikit-optimize, 10 2021.

Ho, J. and Salimans, T. Classifier-free diffusion guidance. *arXiv preprint arXiv:2207.12598*, 2022.

Ho, J., Jain, A., and Abbeel, P. Denoising diffusion probabilistic models. *Advances in neural information processing systems*, 33:6840–6851, 2020.

Hoffmann, M., Scherer, M., Hempel, T., Mardt, A., de Silva, B., Husic, B. E., Klus, S., Wu, H., Kutz, N., Brunton, S. L., and Noé, F. Deeptime: a Python library for machine learning dynamical models from time series data. *ArXiv*, 3(1):1–32, 2021. ISSN 26322153. doi: 10.1088/2632-2153/ac3de0. URL http://arxiv.org/abs/2110.15013.

Honda, S., Yamasaki, K., Sawada, Y., and Morii, H. 10 residue folded peptide designed by segment statistics. *Structure*, 12(8):1507–1518, 2004.

Hummer, G. and Köfinger, J. Bayesian ensemble refinement by replica simulations and reweighting. *The Journal of chemical physics*, 143(24), 2015.

Husic, B. E. and Pande, V. S. Markov State Models: From an Art to a Science. *Journal of the American Chemical Society*, 140(7):2386–2396, 2018. ISSN 15205126. doi: 10.1021/jacs.7b12191.

Irwin, R., Tibo, A., Janet, J. P., and Olsson, S. Semlaflow – efficient 3d molecular generation with latent attention and equivariant flow matching. In *The 28th International Conference on Artificial Intelligence and Statistics*, 2025.

Jaynes, E. T. Information theory and statistical mechanics. *Physical review*, 106(4):620, 1957.

Jülich Supercomputing Centre. JUWELS Cluster and Booster: Exascale Pathfinder with Modular Supercomputing Architecture at Juelich Supercomputing Centre. *Journal of large-scale research facilities*, 7(A138), 2021. doi: 10.17815/jlsrf-7-183.

Kabsch, W. A solution for the best rotation to relate two sets of vectors. *Acta Crystallographica Section A: Crystal Physics, Diffraction, Theoretical and General Crystallography*, 32(5):922–923, 1976.

Kawar, B., Elad, M., Ermon, S., and Song, J. Denoising diffusion restoration models. *Advances in Neural Information Processing Systems*, 35:23593–23606, 2022.

Klein, L., Krämer, A., and Noé, F. Equivariant flow matching. *Advances in Neural Information Processing Systems*, 36:59886–59910, 2023.

Klein, L., Foong, A., Fjelde, T., Mlodozeniec, B., Brockschmidt, M., Nowozin, S., Noé, F., and Tomioka, R. Timewarp: Transferable acceleration of molecular dynamics by learning time-coarsened dynamics. *Advances in Neural Information Processing Systems*, 36, 2024a.

Klein, L., Krämer, A., and Noé, F. Equivariant flow matching. *Advances in Neural Information Processing Systems*, 36, 2024b.

Köhler, J., Klein, L., and Noe, F. Equivariant flows: Exact likelihood generative learning for symmetric densities. In *Proceedings of the 37th International Conference on Machine Learning*, volume 119 of *Proceedings of Machine Learning Research*, pp. 5361–5370. PMLR, 13–18 Jul 2020.

Kolloff, C. and Olsson, S. Rescuing off-equilibrium simulation data through dynamic experimental data with dynAMMo. *Machine Learning: Science and Technology*, 4(4), 2023. ISSN 26322153. doi: 10.1088/2632-2153/ad10ce.

Kolloff, C. and Olsson, S. Machine Learning in Molecular Dynamics Simulations of Biomolecular Systems. *Comprehensive Computational Chemistry*, 3:475–492, 2024. doi: 10.1016/b978-0-12-821978-2.00089-1.

Kolloff, C., Mazur, A., Marzinek, J. K., Bond, P. J., Olsson, S., and Hiller, S. Motional clustering in supra-τc conformational exchange influences noe cross-relaxation rate. *Journal of Magnetic Resonance*, 338:107196, 2022.

Léonard, C. Some properties of path measures. *Séminaire de Probabilités XLVI*, pp. 207–230, 2014.

Lindorff-Larsen, K., Best, R. B., DePristo, M. A., Dobson, C. M., and Vendruscolo, M. Simultaneous determination of protein structure and dynamics. *Nature*, 433(7022): 128–132, January 2005. ISSN 1476-4679.

Lindorff-Larsen, K., Piana, S., Dror, R. O., and Shaw, D. E. How fast-folding proteins fold. *Science*, 334(6055):517–520, 2011.

Lipman, Y., Chen, R. T., Ben-Hamu, H., Nickel, M., and Le, M. Flow matching for generative modeling. *arXiv preprint arXiv:2210.02747*, 2022.

Lipman, Y., Chen, R. T. Q., Ben-Hamu, H., Nickel, M., and Le, M. Flow matching for generative modeling. In *The Eleventh International Conference on Learning Representations*, 2023.

Liu, B., Boysen, J. G., Unarta, I. C., Du, X., Li, Y., and Huang, X. Exploring transition states of protein conformational changes via out-of-distribution detection in the hyperspherical latent space. *Nature Communications*, 16 (1):349, 2025.

Liu, Q. Rectified flow: A marginal preserving approach to optimal transport. *arXiv preprint arXiv:2209.14577*, 2022.

Maoutsa, D., Reich, S., and Opper, M. Interacting particle solutions of fokker–planck equations through gradient–log–density estimation. *Entropy*, 22(8):802, July 2020. ISSN 1099-4300.

Metzner, P., Schütte, C., and Vanden-Eijnden, E. Transition path theory for markov jump processes. *Multiscale Modeling & Simulation*, 7(3):1192–1219, January 2009. ISSN 1540-3467. doi: 10.1137/070699500. URL http://dx.doi.org/10.1137/070699500.

Midgley, L. I., Stimper, V., Antoran, J., Mathieu, E., Schölkopf, B., and Hernández-Lobato, J. M. SE(3) equivariant augmented coupling flows. In *Thirty-seventh Conference on Neural Information Processing Systems*, 2023.

Moqvist, S., Chen, W., Schreiner, M., Nüske, F., and Olsson, S. Thermodynamic interpolation: A generative approach to molecular thermodynamics and kinetics. *Journal of Chemical Theory and Computation*, February 2025. ISSN 1549-9626.

Neklyudov, K., Brekelmans, R., Severo, D., and Makhzani, A. Action matching: Learning stochastic dynamics from samples. In Krause, A., Brunskill, E., Cho, K., Engelhardt, B., Sabato, S., and Scarlett, J. (eds.), *Proceedings of the 40th International Conference on Machine Learning*, volume 202 of *Proceedings of Machine Learning Research*, pp. 25858–25889. PMLR, 23–29 Jul 2023a.

Neklyudov, K., Brekelmans, R., Tong, A., Atanackovic, L., Liu, Q., and Makhzani, A. A computational framework for solving wasserstein lagrangian flows, 2023b.

Nichol, A., Dhariwal, P., Ramesh, A., Shyam, P., Mishkin, P., McGrew, B., Sutskever, I., and Chen, M. Glide: Towards photorealistic image generation and editing with text-guided diffusion models. *arXiv preprint arXiv:2112.10741*, 2021.

Noé, F., Olsson, S., Köhler, J., and Wu, H. Boltzmann generators: Sampling equilibrium states of many-body systems with deep learning. *Science*, 365(6457):eaaw1147, 2019.

Olsson, S., Frellsen, J., Boomsma, W., Mardia, K. V., and Hamelryck, T. Inference of structure ensembles of flexible biomolecules from sparse, averaged data. *PloS one*, 8 (11):e79439, 2013.

Olsson, S., Strotz, D., Vögeli, B., Riek, R., and Cavalli, A. The dynamic basis for signal propagation in human pin1-ww. *Structure*, 24(9):1464–1475, 2016.

Olsson, S., Wu, H., Paul, F., Clementi, C., and Noé, F. Combining experimental and simulation data of molecular processes via augmented Markov models. *Proceedings of the National Academy of Sciences of the United States of America*, 114(31):8265–8270, 2017. ISSN 10916490.

Pande, V. S., Beauchamp, K., and Bowman, G. R. Everything you wanted to know about Markov State Models but were afraid to ask. *Methods*, 52(1):99–105, 2010. ISSN 10462023. doi: 10.1016/j.ymeth.2010.06.002. URL http://dx.doi.org/10.1016/j.ymeth.2010.06.002.

Papamakarios, G., Nalisnick, E., Rezende, D. J., Mohamed, S., and Lakshminarayanan, B. Normalizing flows for probabilistic modeling and inference. *Journal of Machine Learning Research*, 22(57):1–64, 2021.

Pasarkar, A. P., Bencomo, G. M., Olsson, S., and Dieng, A. B. Vendi sampling for molecular simulations: Diversity as a force for faster convergence and better exploration. *The Journal of chemical physics*, 159(14), 10 2023. ISSN 1089-7690 (Electronic). doi: 10.1063/5.0166172.

Pérez-Hernández, G., Paul, F., Giorgino, T., De Fabritiis, G., and Noé, F. Identification of slow molecular order parameters for markov model construction. *The Journal of chemical physics*, 139(1), 2013.

Pitera, J. W. and Chodera, J. D. On the use of experimental observations to bias simulated ensembles. *Journal of chemical theory and computation*, 8(10):3445–3451, 2012.

Plainer, M., Stärk, H., Bunne, C., and Günnemann, S. Transition path sampling with boltzmann generator-based mcmc moves. *arXiv preprint arXiv:2312.05340*, 2023.

Prinz, J.-H., Wu, H., Sarich, M., Keller, B., Senne, M., Held, M., Chodera, J. D., Schütte, C., and Noé, F. Markov models of molecular kinetics: Generation and validation. *The Journal of chemical physics*, 134(17), 2011.

Roux, B. and Weare, J. On the statistical equivalence of restrained-ensemble simulations with the maximum entropy method. *The Journal of chemical physics*, 138(8), 2013.

Satoh, D., Shimizu, K., Nakamura, S., and Terada, T. Folding free-energy landscape of a 10-residue mini-protein, chignolin. *FEBS letters*, 580(14):3422–3426, 2006.

Schreiner, M., Winther, O., and Olsson, S. Implicit transfer operator learning: Multiple time-resolution models for molecular dynamics. In *Thirty-seventh Conference on Neural Information Processing Systems*, 2023.

Shaul, N., Chen, R. T. Q., Nickel, M., Le, M., and Lipman, Y. On kinetic optimal probability paths for generative models. In Krause, A., Brunskill, E., Cho, K., Engelhardt, B., Sabato, S., and Scarlett, J. (eds.), *Proceedings of the 40th International Conference on Machine Learning*, volume 202 of *Proceedings of Machine Learning Research*, pp. 30883–30907. PMLR, 23–29 Jul 2023.

Song, J., Zhang, Q., Yin, H., Mardani, M., Liu, M.-Y., Kautz, J., Chen, Y., and Vahdat, A. Loss-guided diffusion models for plug-and-play controllable generation. In *International Conference on Machine Learning*, pp. 32483–32498. PMLR, 2023.

Song, Y., Sohl-Dickstein, J., Kingma, D. P., Kumar, A., Ermon, S., and Poole, B. Score-based generative modeling through stochastic differential equations. *arXiv preprint arXiv:2011.13456*, 2020.

Tan, C. B., Bose, A. J., Lin, C., Klein, L., Bronstein, M. M., and Tong, A. Scalable equilibrium sampling with sequential boltzmann generators, 2025.

Tang, W. Fine-tuning of diffusion models via stochastic control: entropy regularization and beyond. *arXiv preprint arXiv:2403.06279*, 2024.

Tarvainen, A. and Valpola, H. Mean teachers are better role models: Weight-averaged consistency targets improve semi-supervised deep learning results. *Advances in neural information processing systems*, 30, 2017.

Tong, A., Huang, J., Wolf, G., van Dijk, D., and Krishnaswamy, S. Trajectorynet: A dynamic optimal transport network for modeling cellular dynamics, 2020.

Tong, A., Malkin, N., Huguet, G., Zhang, Y., Rector-Brooks, J., Fatras, K., Wolf, G., and Bengio, Y. Improving and generalizing flow-based generative models with minibatch optimal transport. *ArXiv*, pp. 1–29, 2023.

Uehara, M., Zhao, Y., Black, K., Hajiramezanali, E., Scalia, G., Diamant, N. L., Tseng, A. M., Biancalani, T., and Levine, S. Fine-tuning of continuous-time diffusion models as entropy-regularized control. *arXiv preprint arXiv:2402.15194*, 2024.

Vaswani, A. Attention is all you need. *Advances in Neural Information Processing Systems*, 2017.

Wallace, B., Dang, M., Rafailov, R., Zhou, L., Lou, A., Purushwalkam, S., Ermon, S., Xiong, C., Joty, S., and Naik, N. Diffusion model alignment using direct preference optimization. In *Proceedings of the IEEE/CVF Conference on Computer Vision and Pattern Recognition*, pp. 8228–8238, 2024.

White, A. D. and Voth, G. A. Efficient and minimal method to bias molecular simulations with experimental data. *Journal of chemical theory and computation*, 10(8):3023–3030, 2014.

Øksendal, B. *Stochastic Differential Equations: An Introduction with Applications*. Springer, 6th edition, 2003.

A. Proofs

A.1. Short Derivation of Maximum Entropy Reweighting of MD Trajectories using Observables

The maximum entropy approach (Jaynes, 1957) has been widely adopted (Hummer & Köfinger, 2015; Boomsma et al., 2014; Olsson et al., 2016; 2017; Bottaro et al., 2020) to derive reweighting schemes to find a minimally biased probability distribution that satisfies experimental constraints.

Consider a reference probability distribution $p(\mathbf{x})$, e.g., an empirical distribution estimated from MD simulation data, and an unknown target distribution $p'(\mathbf{x})$ that should match experimental measurements. Following Jaynes' maximum entropy principle, we seek to minimize the KL divergence from $p(\mathbf{x})$ to $p'(\mathbf{x})$ subject to the constraint that the expectations of observables $O_i(\mathbf{x})$ under $p'(\mathbf{x})$ match their experimental values o_i. That is,

$$\min_{p'} \int p'(\mathbf{x}) \log \frac{p'(\mathbf{x})}{p(\mathbf{x})} \, \mathrm{d}\mathbf{x} \tag{23}$$

subject to:

$$\mathbb{E}_{p'(\mathbf{x})}[O_i(\mathbf{x})] = o_i \quad \text{for } i = 1, \ldots, M \tag{24}$$

$$\int p'(\mathbf{x}) \, \mathrm{d}\mathbf{x} = 1 \tag{25}$$

Using the method of Lagrange multipliers, we obtain the following objective:

$$S = -\int p'(\mathbf{x}) \log \frac{p'(\mathbf{x})}{p(\mathbf{x})} \, \mathrm{d}\mathbf{x} + \sum_{i=1}^{M} \lambda_i \left(\int p'(\mathbf{x}) O_i(\mathbf{x}) \, \mathrm{d}\mathbf{x} - o_i \right) + \mu \left(\int p'(\mathbf{x}) \, \mathrm{d}\mathbf{x} - 1 \right) \tag{26}$$

where $\{\lambda_i\}_{i=1}^{M}$ are the Lagrange multipliers for the constraints on the M observables, and μ is the multiplier for density normalization. Setting the functional derivative $\delta S / \delta p'$ to zero yields

$$-\log \frac{p'(\mathbf{x})}{p(\mathbf{x})} - 1 + \sum_{i=1}^{M} \lambda_i O_i(\mathbf{x}) + \mu = 0 \, . \tag{27}$$

Finally, solving for $p'(\mathbf{x})$ and determining μ through normalization gives

$$p'(\mathbf{x}) \propto p(\mathbf{x}) \exp\left(-\sum_{i=1}^{M} \lambda_i O_i(\mathbf{x}) \right) \, , \tag{28}$$

where the λs are determined, e.g., following Bottaro et al. (2020), such that the constraints on the expectations are satisfied. This reweighted distribution represents the maximum entropy solution that satisfies the experimental constraints while minimizing the bias introduced relative to the reference distribution $p(\mathbf{x})$.

A.2. Bounding the Wasserstein distance

In this section, we derive an upper bound on the squared Wasserstein distance $W_2^2(p_0, p_0')$, where the distributions p_0 and p_0' are obtained by evolving a common terminal distribution $p_1 = p_1'$ backward in time according to the ODEs in Equations (5) and (10). We begin by proving a Grönwall-type lemma (see, e.g., Bressan & Piccoli (2007, Lemma 2.1.2)) that will be useful to prove our result.

Lemma A.1. *Let $T > 0$ and let f be an absolutely continuous function over $[0, T]$ satisfying the differential inequality*

$$\frac{\mathrm{d}}{\mathrm{d}t} f(t) \leq a(t) f(t) + b(t) \qquad \textit{for a.e. } t \in [0, T], \tag{29}$$

where $a, b \in L^1([0, T])$ are integrable functions. Then, for every $t \in [0, T]$,

$$f(t) \leq \exp\left(\int_0^t a(u) \, \mathrm{d}u \right) f(0) + \int_0^t \exp\left(\int_s^t a(u) \, \mathrm{d}u \right) b(s) \, \mathrm{d}s \, . \tag{30}$$

Proof. Define the absolutely continuous function

$$\psi(t) \coloneqq \exp\left(-\int_0^t a(u)\,\mathrm{d}u\right)$$

and note that $\psi(t) > 0$, $\psi(0) = 1$, and

$$\frac{\mathrm{d}}{\mathrm{d}t}\psi(t) = -a(t)\psi(t)\ .$$

Multiplying both sides of Equation (29) by $\psi(t)$ and integrating from 0 to t, we have

$$\int_0^t \psi(s)\frac{\mathrm{d}}{\mathrm{d}s}f(s)\,\mathrm{d}s \le \int_0^t \psi(s)a(s)f(s)\,\mathrm{d}s + \int_0^t \psi(s)b(s)\,\mathrm{d}s \tag{31}$$

$$\psi(t)f(t) - \psi(0)f(0) - \int_0^t \psi'(s)f(s)\,\mathrm{d}s \le \int_0^t \psi(s)a(s)f(s)\,\mathrm{d}s + \int_0^t \psi(s)b(s)\,\mathrm{d}s \tag{32}$$

$$\psi(t)f(t) - f(0) + \int_0^t a(s)\psi(s)f(s)\,\mathrm{d}s \le \int_0^t \psi(s)a(s)f(s)\,\mathrm{d}s + \int_0^t \psi(s)b(s)\,\mathrm{d}s \tag{33}$$

$$\psi(t)f(t) \le f(0) + \int_0^t \psi(s)b(s)\,\mathrm{d}s\ . \tag{34}$$

We then divide both sides by $\psi(t)$ again to conclude:

$$f(t) \le \frac{f(0)}{\psi(t)} + \int_0^t \frac{\psi(s)}{\psi(t)}b(s)\,\mathrm{d}s \tag{35}$$

$$= \exp\left(\int_0^t a(u)\,\mathrm{d}u\right)f(0) + \int_0^t \exp\left(\int_s^t a(u)\,\mathrm{d}u\right)b(s)\,\mathrm{d}s \tag{36}$$

□

Proposition A.2. *Let $T > 0$, and let $\mathbf{v}, \mathbf{v}' : [0,T] \times \mathbb{R}^d \to \mathbb{R}^d$ be measurable in time and L_t-Lipschitz in space, with L_t integrable. Let p_0 be a probability measure on $\mathbb{R}^d$, and define p_t, p'_t as the pushforwards of p_0 under the flows of the ODEs $\frac{\mathrm{d}\mathbf{x}_t}{\mathrm{d}t} = \mathbf{v}_t(\mathbf{x}_t)$ and $\frac{\mathrm{d}\mathbf{x}'_t}{\mathrm{d}t} = \mathbf{v}'_t(\mathbf{x}'_t)$. Then for all $t \in [0,T]$,*

$$W_2^2(p_t, p'_t) \le \int_0^t \exp\left(t - s + 2\int_s^t L_u\,\mathrm{d}u\right)\mathbb{E}_{\mathbf{x}\sim p'_s}\left[\|\mathbf{v}_s(\mathbf{x}) - \mathbf{v}'_s(\mathbf{x})\|^2\right]\,\mathrm{d}s\ . \tag{37}$$

Proof. Let ϕ_t, ϕ'_t be the flows of the ODEs, i.e., $\mathbf{x}_t = \phi_t(\mathbf{x}_0)$, $\frac{\mathrm{d}\phi_t(\mathbf{x})}{\mathrm{d}t} = \mathbf{v}_t(\phi_t(\mathbf{x}))$, and similarly for $\mathbf{x}'$ and ϕ'_t. Define the coupling:

$$\tilde{\pi}_t \coloneqq (\phi_t, \phi'_t)_* p_0 \in \Gamma(p_t, p'_t)\ , \tag{38}$$

i.e., the pushforward of p_0 through the map $\mathbf{x} \mapsto (\phi_t(\mathbf{x}), \phi'_t(\mathbf{x}))$. By definition of 2-Wasserstein distance, we can write:

$$W_2^2(p_t, p'_t) \le \int \|\mathbf{x} - \mathbf{x}'\|^2\,\mathrm{d}\tilde{\pi}_t(\mathbf{x}, \mathbf{x}') = \mathbb{E}_{(\mathbf{x}_t, \mathbf{x}'_t)\sim\tilde{\pi}_t}\left[\|\mathbf{x}_t - \mathbf{x}'_t\|^2\right] \tag{39}$$

Take any $\mathbf{x}_0, \mathbf{x}'_0 \in \mathbb{R}^d$ and let $\mathbf{x}_t = \phi_t(\mathbf{x}_0)$ and $\mathbf{x}'_t = \phi'_t(\mathbf{x}'_0)$. Then,

$$\frac{\mathrm{d}}{\mathrm{d}t}\|\mathbf{x}_t - \mathbf{x}'_t\|^2 = 2(\mathbf{x}_t - \mathbf{x}'_t)\cdot(\mathbf{v}_t(\mathbf{x}_t) - \mathbf{v}'_t(\mathbf{x}'_t)) \tag{40}$$

$$= 2(\mathbf{x}_t - \mathbf{x}'_t)\cdot(\mathbf{v}_t(\mathbf{x}_t) - \mathbf{v}_t(\mathbf{x}'_t)) + 2(\mathbf{x}_t - \mathbf{x}'_t)\cdot(\mathbf{v}_t(\mathbf{x}'_t) - \mathbf{v}'_t(\mathbf{x}'_t)) \tag{41}$$

We bound the first term using the Cauchy–Schwarz inequality and the L_t-Lipschitzness of $\mathbf{v}_t$:

$$2(\mathbf{x}_t - \mathbf{x}'_t)\cdot(\mathbf{v}_t(\mathbf{x}_t) - \mathbf{v}_t(\mathbf{x}'_t)) \le 2\|\mathbf{x}_t - \mathbf{x}'_t\|\,\|\mathbf{v}_t(\mathbf{x}_t) - \mathbf{v}_t(\mathbf{x}'_t)\| \tag{42}$$

$$\le 2L_t\|\mathbf{x}_t - \mathbf{x}'_t\|^2\ . \tag{43}$$

Using $0 \leq \|\mathbf{a}-\mathbf{b}\|^2 = \|\mathbf{a}\|^2 + \|\mathbf{b}\|^2 - 2\mathbf{a}\cdot\mathbf{b}$ for the second term we have:

$$2(\mathbf{x}_t - \mathbf{x}'_t)\cdot(\mathbf{v}_t(\mathbf{x}'_t) - \mathbf{v}'_t(\mathbf{x}'_t)) \leq \|\mathbf{x}_t - \mathbf{x}'_t\|^2 + \|\mathbf{v}_t(\mathbf{x}'_t) - \mathbf{v}'_t(\mathbf{x}'_t)\|^2 \,. \tag{44}$$

Plugging these two bounds into Equation (41), we get

$$\begin{aligned}
\frac{\mathrm{d}}{\mathrm{d}t}\|\mathbf{x}_t - \mathbf{x}'_t\|^2 &= 2(\mathbf{x}_t - \mathbf{x}'_t)\cdot(\mathbf{v}_t(\mathbf{x}_t) - \mathbf{v}_t(\mathbf{x}'_t)) + 2(\mathbf{x}_t - \mathbf{x}'_t)\cdot(\mathbf{v}_t(\mathbf{x}'_t) - \mathbf{v}'_t(\mathbf{x}'_t)) && (45)\\
&\leq 2L_t\|\mathbf{x}_t - \mathbf{x}'_t\|^2 + \|\mathbf{x}_t - \mathbf{x}'_t\|^2 + \|\mathbf{v}_t(\mathbf{x}'_t) - \mathbf{v}'_t(\mathbf{x}'_t)\|^2 && (46)\\
&= (2L_t + 1)\|\mathbf{x}_t - \mathbf{x}'_t\|^2 + \|\mathbf{v}_t(\mathbf{x}'_t) - \mathbf{v}'_t(\mathbf{x}'_t)\|^2 \,. && (47)
\end{aligned}$$

Finally, taking expectations on both sides w.r.t. $(\mathbf{x}_t, \mathbf{x}'_t) \sim \tilde{\pi}_t$, and exchanging expectation and derivative under standard regularity assumptions, we get:

$$\frac{\mathrm{d}}{\mathrm{d}t}\mathbb{E}\left[\|\mathbf{x}_t - \mathbf{x}'_t\|^2\right] \leq (2L_t + 1)\,\mathbb{E}\left[\|\mathbf{x}_t - \mathbf{x}'_t\|^2\right] + \mathbb{E}\left[\|\mathbf{v}_t(\mathbf{x}'_t) - \mathbf{v}'_t(\mathbf{x}'_t)\|^2\right] \,. \tag{48}$$

This inequality can be expressed as

$$\frac{\mathrm{d}f(t)}{\mathrm{d}t} \leq (2L_t + 1)f(t) + b(t)\,, \qquad f(0) = 0\,, \tag{49}$$

with

$$\begin{aligned}
f(t) &\coloneqq \mathbb{E}_{(\mathbf{x}_t, \mathbf{x}'_t)\sim\tilde{\pi}_t}\left[\|\mathbf{x}_t - \mathbf{x}'_t\|^2\right] && (50)\\
b(t) &\coloneqq \mathbb{E}_{\mathbf{x}'_t\sim p'_t}\left[\|\mathbf{v}_t(\mathbf{x}'_t) - \mathbf{v}'_t(\mathbf{x}'_t)\|^2\right] \,. && (51)
\end{aligned}$$

Applying Lemma A.1 with $a(t) = (2L_t + 1)$, we get:

$$\begin{aligned}
f(t) &\leq \int_0^t \exp\left(\int_s^t (2L_u + 1)\,\mathrm{d}u\right) b(s)\,\mathrm{d}s && (52)\\
&= \int_0^t e^{t-s}\exp\left(2\int_s^t L_u\,\mathrm{d}u\right) b(s)\,\mathrm{d}s && (53)
\end{aligned}$$

Since from Equation (39) we know that $W_2^2(p_t, p'_t) \leq f(t)$, the statement follows:

$$W_2^2(p_t, p'_t) \leq \int_0^t e^{t-s}\exp\left(2\int_s^t L_u\,\mathrm{d}u\right)\mathbb{E}_{\mathbf{x}\sim p'_s}\left[\|\mathbf{v}_s(\mathbf{x}) - \mathbf{v}'_s(\mathbf{x})\|^2\right]\,\mathrm{d}s\,. \tag{54}$$

□

Although the result in the time-reversed case is straightforward as it directly follows from a time reparameterization, we state it and prove it for the sake of completeness.

Proposition A.3. *Let $\mathbf{v}, \mathbf{v}' : [0,1]\times\mathbb{R}^d \to \mathbb{R}^d$ be measurable in time and L_t-Lipschitz in space, with L_t integrable. Let p_0, p'_0 be probability measures on $\mathbb{R}^d$, and define p_t, p'_t as the pushforwards of p_0 under the flows of the ODEs $\frac{\mathrm{d}\mathbf{x}_t}{\mathrm{d}t} = \mathbf{v}_t(\mathbf{x}_t)$ and $\frac{\mathrm{d}\mathbf{x}'_t}{\mathrm{d}t} = \mathbf{v}'_t(\mathbf{x}'_t)$. Assume $p_1 = p'_1$. Then,*

$$W_2^2(p_0, p'_0) \leq \int_0^1 \exp\left(t + 2\int_0^t L_s\,\mathrm{d}s\right)\mathbb{E}_{\mathbf{x}\sim p'_t}\left[\|\mathbf{v}_t(\mathbf{x}) - \mathbf{v}'_t(\mathbf{x})\|^2\right]\,\mathrm{d}t\,. \tag{55}$$

Proof. Consider the time reversal transformation $s = 1 - t$. Define $\tilde{\mathbf{x}}_s \coloneqq \mathbf{x}_{1-s}$ and $\tilde{\mathbf{x}}'_s \coloneqq \mathbf{x}'_{1-s}$, where $\mathbf{x}_t$ and $\mathbf{x}'_t$ satisfy the original ODEs with vector fields $\mathbf{v}_t, \mathbf{v}'_t$, with $\mathbf{x}_t \sim p_t$, $\mathbf{x}'_t \sim p'_t$, and $p_1 = p'_1$. Differentiating the reversed processes, we get:

$$\frac{\mathrm{d}\tilde{\mathbf{x}}_s}{\mathrm{d}s} = \frac{\mathrm{d}\mathbf{x}_{1-s}}{\mathrm{d}t}\cdot\frac{\mathrm{d}t}{\mathrm{d}s} = -\mathbf{v}_{1-s}(\mathbf{x}_{1-s}) = -\mathbf{v}_{1-s}(\tilde{\mathbf{x}}_s) \tag{56}$$

and similarly for $\tilde{\mathbf{x}}'$. Thus, the reversed processes satisfy:

$$\frac{\mathrm{d}\tilde{\mathbf{x}}_s}{\mathrm{d}s} = \tilde{\mathbf{v}}_s(\tilde{\mathbf{x}}_s)\ , \quad \frac{\mathrm{d}\tilde{\mathbf{x}}'_s}{\mathrm{d}s} = \tilde{\mathbf{v}}'_s(\tilde{\mathbf{x}}'_s)\ , \tag{57}$$

where we defined the reversed velocity fields $\tilde{\mathbf{v}}_s(\mathbf{x}) := -\mathbf{v}_{1-s}(\mathbf{x})$ and $\tilde{\mathbf{v}}'_s(\mathbf{x}) := -\mathbf{v}'_{1-s}(\mathbf{x})$. From the definitions $\tilde{\mathbf{x}}_s := \mathbf{x}_{1-s}$ and $\tilde{\mathbf{x}}'_s := \mathbf{x}'_{1-s}$ it directly follows that $\tilde{p}_s = p_{1-s}$ and $\tilde{p}'_s = p'_{1-s}$. At $s = 0$, we have $\tilde{p}_0 = p_1 = p'_1 = \tilde{p}'_0$, so the reversed processes start from the same distribution.

Since $\mathbf{v}_t$ and $\mathbf{v}'_t$ are L_t-Lipschitz in space with L_t integrable, $\tilde{\mathbf{v}}_s$ and $\tilde{\mathbf{v}}'_s$ are L_{1-s}-Lipschitz. The reversed ODEs start at $s = 0$ from the same distribution ($\tilde{p}_0 = \tilde{p}'_0$) and evolve to $\tilde{p}_1 = p_0$ and $\tilde{p}'_1 = p'_0$ at $s = 1$. Applying Proposition A.2, we get:

$$W_2^2(\tilde{p}_1, \tilde{p}'_1) \leq \int_0^1 \exp\left(1 - s + 2\int_s^1 L_{1-u}\,\mathrm{d}u\right) \mathbb{E}_{\mathbf{x}\sim\tilde{p}'_s}\left[\|\tilde{\mathbf{v}}_s(\mathbf{x}) - \tilde{\mathbf{v}}'_s(\mathbf{x})\|^2\right]\,\mathrm{d}s\ . \tag{58}$$

Substituting $\tilde{p}_s = p_{1-s}$ and $\tilde{p}'_s = p'_{1-s}$, using the definitions of $\tilde{\mathbf{v}}_t, \tilde{\mathbf{v}}'_t$, and applying a change of variables $t = 1 - s$, we obtain the desired bound:

$$W_2^2(p_0, p'_0) \leq \int_0^1 \exp\left(1 - s + 2\int_s^1 L_{1-u}\,\mathrm{d}u\right) \mathbb{E}_{\mathbf{x}\sim p'_{1-s}}\left[\|\mathbf{v}_{1-s}(\mathbf{x}) - \mathbf{v}'_{1-s}(\mathbf{x})\|^2\right]\,\mathrm{d}s \tag{59}$$

$$= \int_0^1 \exp\left(t + 2\int_{1-t}^1 L_{1-u}\,\mathrm{d}u\right) \mathbb{E}_{\mathbf{x}\sim p'_t}\left[\|\mathbf{v}_t(\mathbf{x}) - \mathbf{v}'_t(\mathbf{x})\|^2\right]\,\mathrm{d}t \tag{60}$$

$$= \int_0^1 \exp\left(t + 2\int_0^t L_s\,\mathrm{d}s\right) \mathbb{E}_{\mathbf{x}\sim p'_t}\left[\|\mathbf{v}_t(\mathbf{x}) - \mathbf{v}'_t(\mathbf{x})\|^2\right]\,\mathrm{d}t\ . \tag{61}$$

□

In this work, we are specifically interested in the ODEs (5) and (10):

Proposition 3.1. *Let p_t and p'_t be the distributions at time t obtained by solving the ODEs (5) and (10) backwards in time from the same initial distribution p_1 at $t = 1$. Assume that the vector fields are measurable in time and L_t-Lipschitz in space with L_t integrable. Then:*

$$W_2^2(p_0, p'_0) \leq \int_0^1 w_{\mathrm{W}}(t)\,\frac{g(t)^4}{4}\,\mathbb{E}_{\mathbf{x}\sim p'_t}\left[\|\mathbf{h}_\vartheta(\mathbf{x}, t)\|^2\right]\,\mathrm{d}t, \tag{13}$$

with $w_{\mathrm{W}}(t) := e^{t+2\int_0^t L_s\,\mathrm{d}s}$

Proof. The ODEs (5) and (10) have the following vector fields:

$$\mathbf{v}_t(\mathbf{x}) = \mathbf{f}(\mathbf{x}, t) - \frac{1}{2}g(t)^2\mathbf{s}(\mathbf{x}, t)$$
$$\mathbf{v}'_t(\mathbf{x}) = \mathbf{f}(\mathbf{x}, t) - \frac{1}{2}g(t)^2\left(\mathbf{s}(\mathbf{x}, t) + \mathbf{h}(\mathbf{x}, t)\right)\ .$$

The result directly follows by applying Proposition A.3:

$$W_2^2(p_0, p'_0) \leq \int_0^1 \exp\left(t + 2\int_0^t L_s\,\mathrm{d}s\right)\frac{g(t)^4}{4}\mathbb{E}_{\mathbf{x}\sim p'_t}\left[\|\mathbf{h}_\vartheta(\mathbf{x}, t)\|^2\right]\,\mathrm{d}t\ . \tag{62}$$

□

A.3. Bounding the KL divergence

Proposition A.4. *Let $p, p' : \mathbb{R}^d \times [0, 1] \to \mathbb{R}_{\geq 0}$ be two probability paths over time $t \in [0, 1]$, induced by two reverse-time SDEs:*

$$\mathrm{d}\mathbf{x}_t = \boldsymbol{\mu}_t(\mathbf{x}_t)\,\mathrm{d}t + g_t\,\mathrm{d}\widetilde{\mathbf{w}}_t\ , \qquad \mathrm{d}\mathbf{x}_t = \boldsymbol{\mu}'_t(\mathbf{x}_t)\,\mathrm{d}t + g_t\,\mathrm{d}\widetilde{\mathbf{w}}'_t \tag{63}$$

where $\widetilde{\mathbf{w}}_t, \widetilde{\mathbf{w}}'_t$ are reverse-time Wiener processes, $\boldsymbol{\mu}, \boldsymbol{\mu}' : \mathbb{R}^d \times [0,1] \to \mathbb{R}^d$, and $g : [0,1] \to \mathbb{R}_{>0}$. Assume that $p_1 = p'_1$, that both SDEs admit strong solutions, and that $\mathbb{P}' \ll \mathbb{P}$, where $\mathbb{P}, \mathbb{P}'$ are the path measures induced by the SDEs on $C([0,1], \mathbb{R}^d)$. Then:

$$D_{\mathrm{KL}}(p'_0 \| p_0) \leq \frac{1}{2} \int_0^1 \frac{1}{g_t^2} \, \mathbb{E}_{\mathbf{x} \sim p'_t} \left[\| \boldsymbol{\mu}'_t(\mathbf{x}) - \boldsymbol{\mu}_t(\mathbf{x}) \|^2 \right] \, \mathrm{d}t \, . \tag{64}$$

Proof. By applying the chain rule of the KL divergence (Léonard, 2014, Theorem 2.4) at $t = 0$ and $t = 1$, we have:

$$D_{\mathrm{KL}}(\mathbb{P}' \| \mathbb{P}) = D_{\mathrm{KL}}(p'_0 \| p_0) + \mathbb{E}_{\mathbf{x}_0^* \sim p'_0} \Big[\underbrace{D_{\mathrm{KL}}(\mathbb{P}'_{\mathbf{x}_0 = \mathbf{x}_0^*} \| \mathbb{P}_{\mathbf{x}_0 = \mathbf{x}_0^*})}_{\geq 0} \Big] \tag{65}$$

$$D_{\mathrm{KL}}(\mathbb{P}' \| \mathbb{P}) = \underbrace{D_{\mathrm{KL}}(p'_1 \| p_1)}_{=0} + \mathbb{E}_{\mathbf{x}_1^* \sim p'_1} \left[D_{\mathrm{KL}}(\mathbb{P}'_{\mathbf{x}_1 = \mathbf{x}_1^*} \| \mathbb{P}_{\mathbf{x}_1 = \mathbf{x}_1^*}) \right] \, . \tag{66}$$

The subscripts on the path measures denote conditioning on the value of the process at a specific time (by disintegration of path measures). We can therefore bound $D_{\mathrm{KL}}(p'_0 \| p_0)$ by a KL divergence between path measures:

$$D_{\mathrm{KL}}(p'_0 \| p_0) \leq \mathbb{E}_{\mathbf{x}_1^* \sim p'_1} \left[D_{\mathrm{KL}}(\mathbb{P}'_{\mathbf{x}_1 = \mathbf{x}_1^*} \| \mathbb{P}_{\mathbf{x}_1 = \mathbf{x}_1^*}) \right] \, . \tag{67}$$

By Girsanov's theorem (Øksendal, 2003),

$$D_{\mathrm{KL}}(\mathbb{P}'_{\mathbf{x}_1 = \mathbf{x}_1^*} \| \mathbb{P}_{\mathbf{x}_1 = \mathbf{x}_1^*}) = \frac{1}{2} \mathbb{E}_{\mathbb{P}'_{\mathbf{x}_1 = \mathbf{x}_1^*}} \left[\int_0^1 \frac{1}{g_t^2} \| \boldsymbol{\mu}'_t(\mathbf{x}_t) - \boldsymbol{\mu}_t(\mathbf{x}_t) \|^2 \, \mathrm{d}t \right] \, . \tag{68}$$

We can now write the iterated expectation as an expectation over the unconditional path measure $\mathbb{P}'$:

$$\mathbb{E}_{\mathbf{x}_1^* \sim p'_1} \left[D_{\mathrm{KL}}(\mathbb{P}'_{\mathbf{x}_1 = \mathbf{x}_1^*} \| \mathbb{P}_{\mathbf{x}_1 = \mathbf{x}_1^*}) \right] = \frac{1}{2} \mathbb{E}_{\mathbf{x}_1^* \sim p'_1} \left[\mathbb{E}_{\mathbb{P}'_{\mathbf{x}_1 = \mathbf{x}_1^*}} \left[\int_0^1 \frac{1}{g_t^2} \| \boldsymbol{\mu}'_t(\mathbf{x}_t) - \boldsymbol{\mu}_t(\mathbf{x}_t) \|^2 \, \mathrm{d}t \right] \right] \tag{69}$$

$$= \frac{1}{2} \mathbb{E}_{\mathbb{P}'} \left[\int_0^1 \frac{1}{g_t^2} \| \boldsymbol{\mu}'_t(\mathbf{x}_t) - \boldsymbol{\mu}_t(\mathbf{x}_t) \|^2 \, \mathrm{d}t \right] \, . \tag{70}$$

Finally, we switch the expectation and integral (Fubini–Tonelli), and simplify the expectation over $\mathbb{P}'$ into an expectation over the time marginal p'_t since the argument of the integral only depends on t:

$$\mathbb{E}_{\mathbb{P}'} \left[\int_0^1 \frac{1}{g_t^2} \| \boldsymbol{\mu}'_t(\mathbf{x}_t) - \boldsymbol{\mu}_t(\mathbf{x}_t) \|^2 \, \mathrm{d}t \right] = \int_0^1 \frac{1}{g_t^2} \, \mathbb{E}_{\mathbf{x} \sim p'_t} \left[\| \boldsymbol{\mu}'_t(\mathbf{x}) - \boldsymbol{\mu}_t(\mathbf{x}) \|^2 \right] \, \mathrm{d}t \, , \tag{71}$$

which concludes the proof. □

In this work, we are specifically interested in the reverse-time SDEs (4) and (9):

Proposition 3.2. *Let p_t and p'_t be the distributions at time t induced by the reverse-time SDEs (4) and (9) starting from the same distribution p_1 at $t = 1$. Assume that both SDEs admit strong solutions, and that $\mathbb{P}' \ll \mathbb{P}$, where $\mathbb{P}, \mathbb{P}'$ are the path measures induced by the SDEs on $C([0,1], \mathbb{R}^d)$. Then:*

$$D_{\mathrm{KL}}(p'_0 \| p_0) \leq \int_0^1 w_{\mathrm{KL}}(t) \, \frac{g(t)^4}{4} \, \mathbb{E}_{\mathbf{x} \sim p'_t} \left[\| \mathbf{h}_\vartheta(\mathbf{x}, t) \|^2 \right] \, \mathrm{d}t, \tag{14}$$

with $w_{\mathrm{KL}}(t) \coloneqq \frac{2}{g(t)^2}$

Proof. The result directly follows by applying Proposition A.4 to the drifts of the reverse-time SDEs (4) and (9). □

B. Experimental details

B.1. Coarse-grained Boltzmann Emulator model architecture and training setup

The score function in this work is based on the CPaiNN architecture introduced in (Schreiner et al., 2023) with $n_h = 64$ hidden features and five message passing layers. The score is calculated in two steps - embedding and processing by CPaiNN. In the embedding step, each node is embedded using a lookup function. The pairwise distances between nodes and the diffusion time t is encoded with a positional embedding as described in (Vaswani, 2017). The embedded t is concatenated to the node features and the resulting vector is projected down to n_h dimensions using an MLP. Additionally, each node is assigned n_h zero-vectors serving as initial equivariant features.

The embedded graph is processed by the score model and the final equivariant features are read out as the score.

The score model was trained in a DDPM setup as described in (Schreiner et al., 2023) using an exponential moving average (Tarvainen & Valpola, 2017) with a decay value of 0.99, batch size of 128, and the Adam optimizer with a learning rate of 0.001, $\beta_1 = .9$, $\beta_2 = .999$.

B.2. Analysis of CLN025 MD Trajectory

To evaluate our methods, we calculate pair-wise C^α distances of the ten-residue miniprotein and project those features onto the two slowest time-lagged independent components (Pérez-Hernández et al., 2013) with a lag time $\tau = 10\,\text{ns}$. We then clustered the MD trajectory into $n = 128$ states using KMeans. The discretized trajectory was then used for estimating a Markov State Model (MSM) (Prinz et al., 2011; Bowman et al., 2014; Kolloff & Olsson, 2024) using a lag time of $\tau = 10\,\text{ns}$ (Hoffmann et al., 2021). For detailed discussions on the background and use of these methods, we refer the reader to (Bowman et al., 2009; Pande et al., 2010; Prinz et al., 2011; Husic & Pande, 2018).

B.2.1. Committor Probabilities and Transition States

In order to identify the transition states, we computed the committor probabilities (Metzner et al., 2009), defining transition states as those with values near 0.5. If we consider a reactive process of a system on a space Ω going from a state $A \subset \Omega$ to another state $B \subset \Omega$, s. t. $A \cap B = \emptyset$, the committor q_i describes the probability of reaching state B before A starting from i.(E. & Vanden-Eijnden, 2006) Considering the protein folding process, A is the unfolded state and B is the folded state, $q_i = P(\text{folded first} \mid \text{starting at state i})$. Most importantly in our context, are states with committor values near 0.5, indicating an equal likelihood of folding or unfolding, which are identified as *transition states* (Figure 5). These states often represent critical bottlenecks in the folding process or in chemical reactions and are thus of significant biophysical and chemical interest.

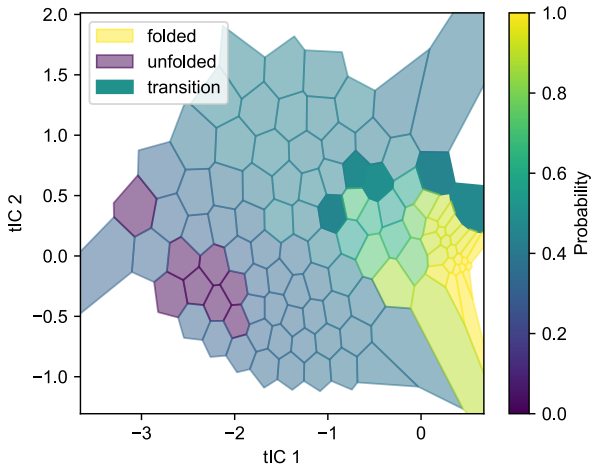

Figure 5: **Committor Probability Voronoi Diagram.** Each region is colored by its committor probability, where values near 1 correspond to folded states and values near 0 correspond to unfolded states. Regions near 0.5 represent transition states.

B.3. Observable Guidance

We evaluated our method on two systems: a synthetic one-dimensional model and the chignolin protein system. For both systems, guidance parameters were optimized using Bayesian optimization with Gaussian Processes (GPs) implemented via scikit-optimize (Head et al., 2021). The scaling function took the form $\eta_t(\vartheta) = \eta_{\text{init}} \exp(-\kappa(1-t))$, with system-specific search spaces for η_{init} and κ. All optimizations used 64 function evaluations with a convergence threshold of 1e-5, retaining the 5 best parameter sets. The scaling hyperparameter γ, which balances observable matching and minimum excess work, was consistently set to 1e-3 after hyperparameter search.

B.3.1. Synthetic System

Neural Network Architecture and Training. Two multilayer perceptron (MLP) networks were trained on the Prinz potential system (Prinz et al., 2011) with $k_\text{B} = 1.38 \cdot 10^{-23}$ and $T = 300$ K: one on the unbiased potential and another

Table 3: Gaussian Mixture Model Component Parameters

Component	Mean (μ)	Variance (σ^2)	Weight (w)
1	0.30	0.01	0.35
2	-0.24	0.01	0.22
3	0.69	0.01	0.27
4	-0.71	0.01	0.16

incorporating a linear bias of -4. Both networks were trained for 15,000 epochs using a batch size of 256 and the Adam optimizer with a learning rate of 1e-3. The networks shared identical architectures, with input dimension corresponding to single-atom ($n_{\text{atoms}} = 1$) one-dimensional data, a time embedding dimension of 3, hidden dimension of 64, and output dimension of 1. The training process employed a linear beta scheduler with parameters $a = 0.1$ and $b = 20.0$. This scheduler controlled the noise scale during training, allowing for progressive refinement of the learned distributions.

Observable Function Parameterization. For the synthetic system, the observable function was implemented as a Gaussian Mixture Model (GMM) with four components, parameterized as shown in Table 3. The Lagrange multiplier was calculated to be -0.66 following (Bottaro et al., 2020). The parameter search space was defined as $\eta_{\text{init}} \in [1.0, 20.0]$ and $\kappa \in [1.0, 20.0]$.

B.3.2. Chignolin System

For the chignolin protein system, we defined the observable function using the interatomic distance between the first and last C^α atoms (C^α_1 and C^α_{10}). The folding free energy was calculated as:

$$\Delta G = -k_B T \log\left(\frac{p_f}{1 - p_f}\right) \tag{72}$$

where p_f represents the fraction of folded samples, defined using a distance cutoff of 7.5 Å. The Lagrange multiplier was determined to be -0.5 (Bottaro et al., 2020). The parameter search space was set to $\eta_{\text{init}} \in [10^{-2}, 1.0]$ and $\kappa \in [1.0, 10.0]$. The optimization process used 256 samples per epoch, with final evaluation conducted on 256×256 samples to ensure robust statistical assessment.

B.3.3. Compute Resources and Runtime Details

Observable guidance experiments were conducted using HPC compute infrastructure equipped with NVIDIA A100 GPUs (80GB memory). Training and evaluation scripts were run on single-GPU nodes.

For the synthetic system (Section 2 and Table 1), each experiment took approximately 4 min to run, consuming 6 GB GPU memory. The chignolin experiments (e.g., Figure 12) required up to 30 min of compute time per run, and 30 GB of GPU memory due to the larger input size and batch requirements. Ablation studies (Figure 9) were conducted with the same hardware and each variant was run across 50 (synthetic case) and 10 (chignolin case) seeds, requiring 1–3 hours per configuration. In total, the reported experiments required approximately 10 GPU hours. Preliminary runs and failed hyperparameter sweeps amounted to an estimated additional 100 GPU hours, not included in the main results.

B.4. Path Guidance

Similar to observable guidance, path and loss guidance were evaluated on two systems: a synthetic two-dimensional setup and the chignolin mini-protein. We experimented with various functional forms for the guiding strength and time-dependent bandwidth and found that sigmoid-like step functions performed well across both tasks:

$$\eta_t(\vartheta) = \vartheta_{init}\,(1 - \sigma(\vartheta_g(t - \vartheta_s))) \tag{73}$$

$$h_t(\varphi) = \varphi_{init} + \sigma(\varphi_g(t - \varphi_s)) \tag{74}$$

To optimize the parameter sets ϑ and φ we applied Bayesian optimization with Gaussian Processes (GPs), using the `scikit-optimize` library. We employed the `gp_hedge` acquisition function, which dynamically combines strategies such as Expected Improvement (EI), Probability of Improvement (PI), and Lower Confidence Bound (LCB) based on their empirical performance. After initial exploration, we restricted the search space to a sensible domain to improve optimization efficiency and support a broader sweep of experimental configurations.

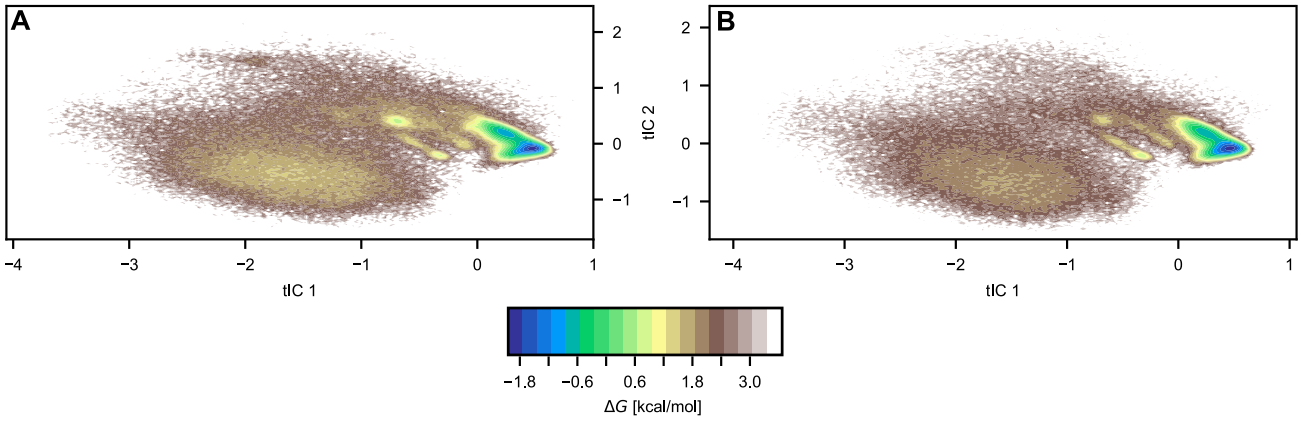

Figure 6: **tICA Projection of Original and Observable-Guided Model.** State space distribution projected onto the first and second tICs for the original (A) and guided (B) BG. The plots are colored by their respective energies.

B.4.1. Synthetic System

We evaluated our method on a simple three-moon example, where the two-dimensional dataset consists of three noisy half-moon arcs generated by sampling from shifted semicircles with optional convexity and added Gaussian noise (see Figure 10). While two of the arcs are well-represented in the training data, only 2.5% of the samples belong to the third arc, creating a challenging low-data region. We adopt the Conditional Flow Matching (CFM) framework (Lipman et al., 2022), from which the score function can be derived for augmentation. To approximate the resulting vector field, we train a four-layer MLP on 10,000 samples for 3,000 steps using a learning rate of 10^{-4} and a batch size of 256. Training hyperparameters were selected via a small grid search on an NVIDIA A100 GPU. For optimizing the guidance schedules in Equation (73), we run 25 Bayesian optimization steps. To classify whether a sample falls within the target moon, we train a two-layer MLP classifier using a learning rate of 10^{-3}, 1,000 training steps, and a batch size of 256. For path and loss guidance, we evaluated γ values between 0 and 1, finding 0.03 working best for path guidance and 0.1 for loss guidance. For sampling we use 20 guiding points generating 1000 samples in one batch.

B.4.2. Chignolin System

The Boltzmann Emulator used for sampling the chignolin system is described in Appendix B.1. Since loss guidance could not be reliably optimized via Bayesian optimization, we performed an extensive grid search over hyperparameters, including various functional forms for the schedules in Equation (73). This grid search was run for 24 hours on a single NVIDIA H100 GPU and served primarily to investigate the failure modes of loss guidance. The corresponding results are shown in Figure 12B. To improve stability, we explored gradient clipping and found it essential for loss guidance. For MEW-guided optimization, we focused exclusively on path guidance. We tested γ values between 0 and 1 and found values $\gamma \leq 0.5$ to be effective. Each run consisted of 50 Bayesian optimization steps, with one function evaluation taking approximately 2.5 minutes. As a result, a full optimization run for a fixed γ required about two hours on a single NVIDIA H100 GPU (80GB). After each iteration, we computed committor probabilities of the sampled protein conformations using the method described in Appendix B.2 to estimate the proportion of transition-state configurations. For each of the 50 guiding points available, we generated 10 samples, leading to a sample batch size of 500.

C. Results: Observable Guidance

All error bars for observable guidance were calculated as the standard deviation between n runs ($n = 50$ for the 1D energy potential experiments and $n = 10$ for the chignolin experiments.

C.1. Ablation Studies

D. Results: Path Guidance

D.1. Synthetic System

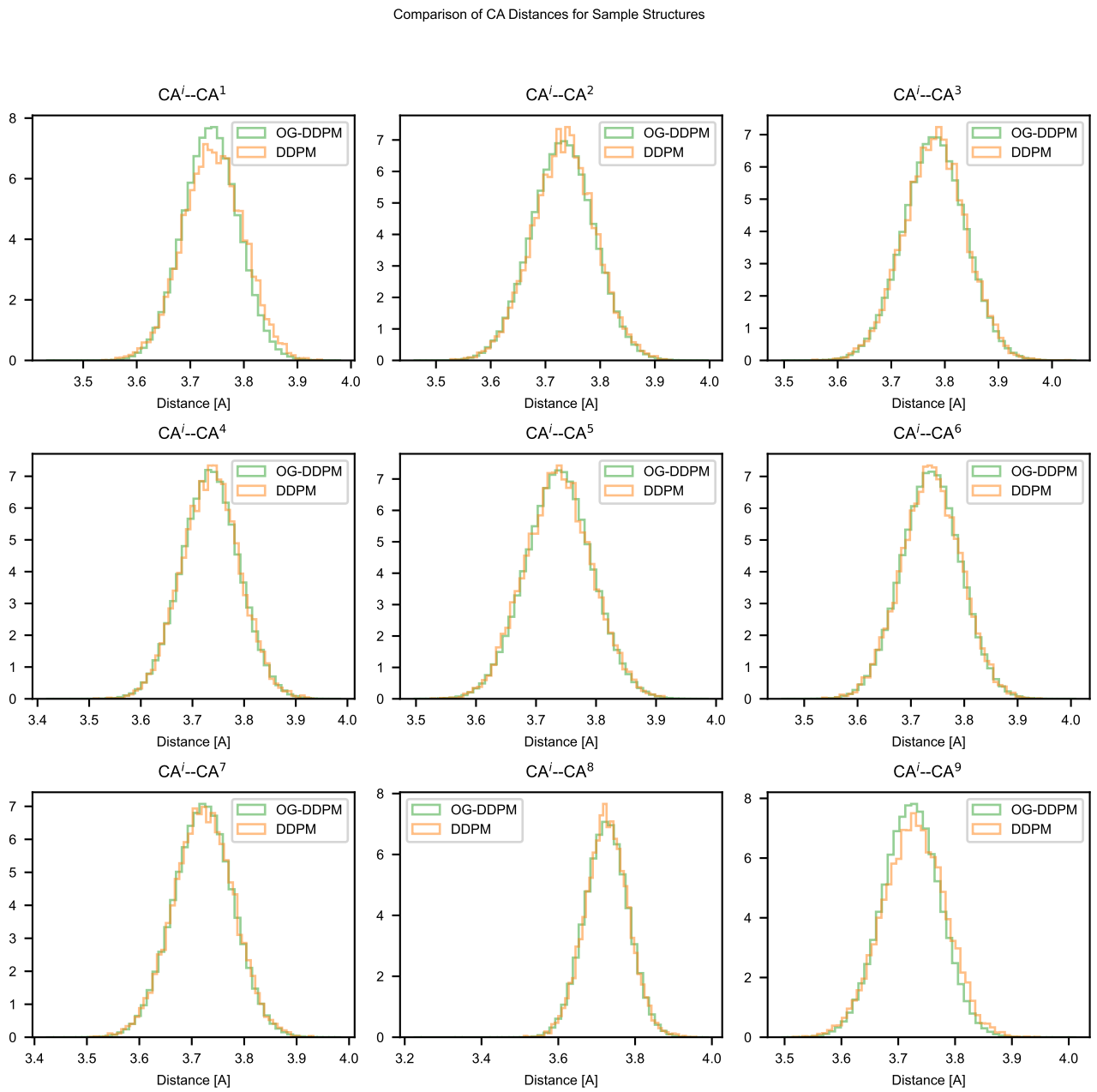

Figure 7: **Comparison of sequential C^α–C^α distances between the observable-guided diffusion model (OG-DDPM, green) and the original diffusion model (DDPM, orange).** The plots show the distance distributions for all adjacent C^α pairs (0–2 through 8–9 using zero indexing) in the protein backbone, showing that the guided model maintains proper protein geometry while achieving the desired constraints.

Table 4: Metrics for $O(\mathbf{x})$ and KL divergence with and without MEW regularization.

Model $\mathcal{M}$	$\mathbb{E}_{p_{\mathcal{M}}(\mathbf{x})}[O(\mathbf{x})]$	$\mathrm{KL}[p_{\mathrm{GT}}(\mathbf{x})\|p_{\mathcal{M}}(\mathbf{x})]$
w/o MEW	0.131	0.754 ± 1.533
w/ MEW	0.131	0.029 ± 0.007

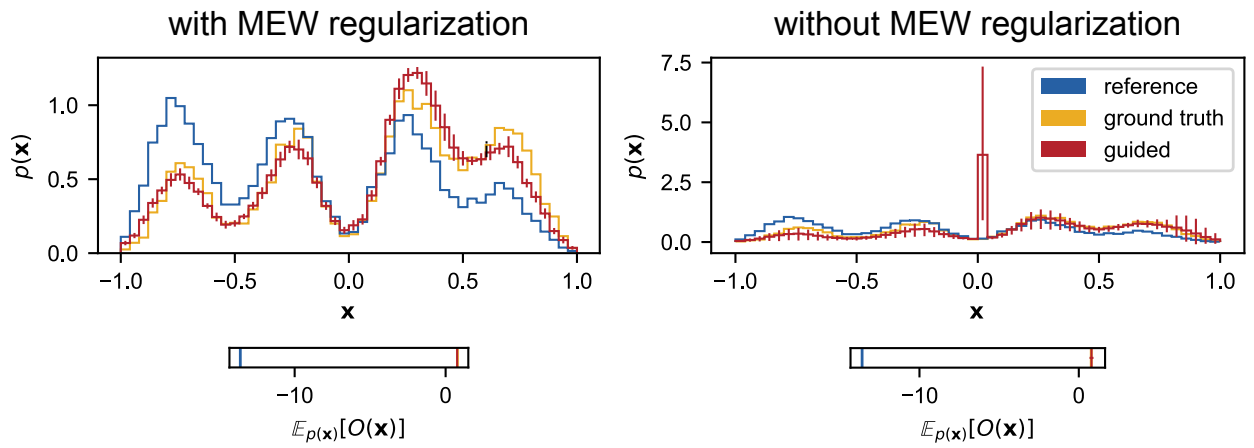

Figure 9: **Ablation study on MEW regularization in the 1D four-well potential.** Left: With MEW regularization, the guided distribution (red) closely matches both the reference (blue) and ground truth (yellow) distributions. Right: without regularization, guidance leads to mode collapse and overconcentration, resulting in low observable prediction error but poor distributional fidelity. Insets show the expected observable values $\mathbb{E}_{p(\mathbf{x})}[O(\mathbf{x})]$.

Before applying our method to the Boltzmann Generator on the chignolin system, we first evaluated it on a simple three-moon example (Figure 10; see Appendix B.4.1 for implementation details). This setup offers a useful testbed, as the low-data region is connected to a high-density area while remaining well-separated from the other half-moon. The objective of guidance in this case is to enable transitions into the low-density region without deviating off the underlying data manifold connecting the moons.

We observe that with ODE sampling, points frequently fall off the manifold, and only careful tuning of the guiding strength minimizes this issue. In contrast, SDE guiding is more robust, as noise helps correct guidance errors. Overall, after minimal optimization of η_t and h_t, both Path Guidance and Loss Guidance perform well on this toy example. However, in both methods, careful calibration of the guiding strength at low t is essential, as errors at this stage cannot be corrected later. Hence, we found the sigmoid function to be effective in these scenarios, as it naturally converges to 0 for $t \to 1$. In contrast to the Chingolin experiment, we find that loss guidance performs equally well in this synthetic setting, likely due to the simplicity of the data distribution, where the (KDE) in data space sufficiently captures the underlying probability distribution. We also investigate the effect of MEW regularization and observe that omitting the regularization reduces the diversity of the generated samples. Without MEW, the samples tend to be overly guided towards the guiding points on most probable regions, failing to capture the full variance of the underlying distribution Figure 11.

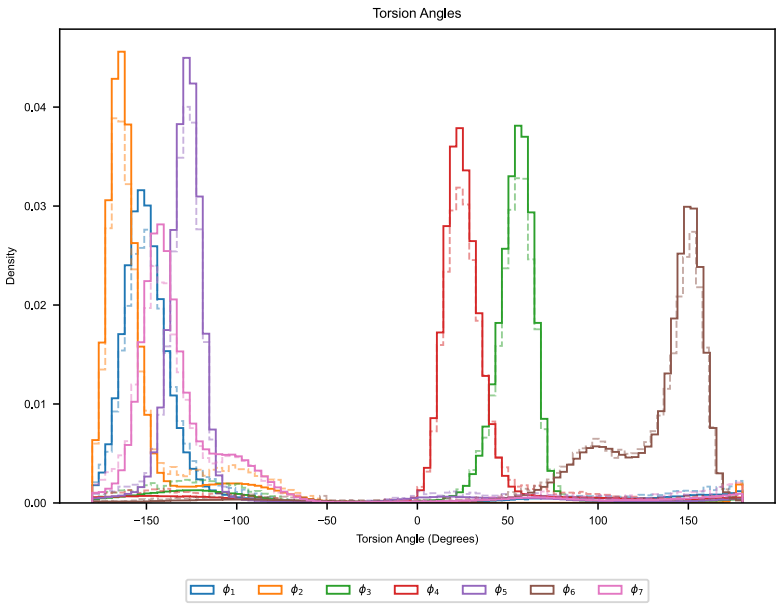

Figure 8: **Distribution of backbone torsion angles (ϕ_1 through ϕ_7) comparing the MD simulation (solid lines) with the observable-guided model (dashed lines).** The close agreement between the distributions indicates that the guided model preserves the native conformational preferences of the protein while satisfying the experimental constraints. Each torsion angle is shown in a different color. The differences between the two densities stem from the guidance procedure. Importantly, the the torsion angles themselves remain the same.

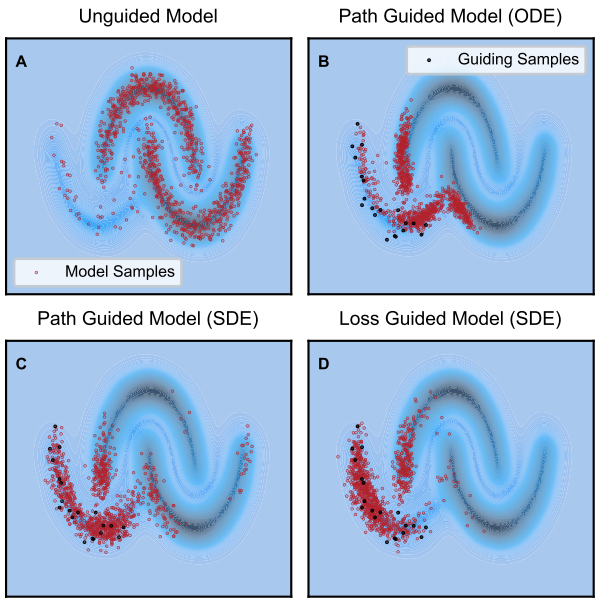

Figure 10: **Sampling the synthetic system.** Comparison of unguided, path-guided, and loss-guided models using both SDE and ODE samplers.

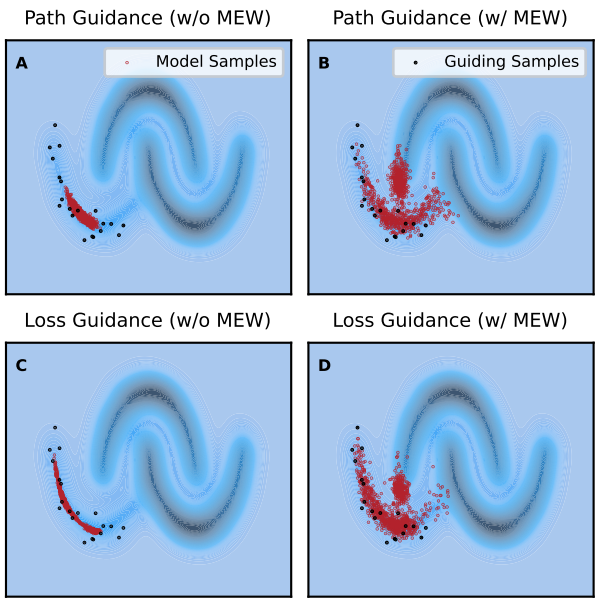

Figure 11: **Guidance with and without MEW regularization**. MEW guidance ensures that we do not collapse onto the guiding points.

D.2. Ablation Studies on Loss guidance

Since reliable sampling with loss guidance could not be achieved, we conducted a more thorough investigation to enable a fair comparison. Instead of relying on Bayesian optimization, we performed an extensive grid search over the guiding parameters (see Appendix B.4.2 for details), with particular focus on smaller guiding strengths to mitigate the effects of unstable or misaligned gradients. Compared to path guidance, the grid search results show substantially lower guiding success, with a maximum transition-state sampling rate of only 0.15%. While this does represent an improvement over unguided sampling (1%), most configurations with non-negligible guidance success resulted in degenerate samples (Figure 12B). Our analysis suggests that while loss guidance can partially align the model with the target angle distribution, it struggles to follow the desired sampling trajectory throughout the generative process. As a result, strong corrections near the data distribution are required, increasing the risk of sample degeneration (Figure 12A).

D.3. Baseline Experiments

In this section, we describe the other two baselines, mentioned in Section 4.2, which do not augment the vector field. Instead, they utilize the latent representations of the guiding points $\mathcal{X}_t^g$ to initialize the sampling process for generating new points with similar latent characteristics. While these methods are appealing in their simplicity, they lack direct control over the sampling process itself.

Latent-KDE (L-KDE). We can fit a KDE in the latent space on $\mathcal{X}_1^g$, sample from it, and integrate the probability flow ODE backwards in time. Fitting the KDE at the prior can be advantageous because the Euclidean distance, on which most kernels are based, is better suited for Gaussian-distributed data compared to its use in data space. We refer to this method as Latent-KDE (L-KDE).

Stochastic-Reverse (SR). Alternatively, we can select a specific time step t such that the desired properties are preserved and initialize the backward SDE (Equation (2)) with latents from $\mathcal{X}_t^g$. The stochasticity of the SDE will ensure we generate new divers samples with $\mathbf{x}' \in A$.

We conduct sampling experiments using the aforementioned baseline methods to verify whether the results align with our intuition. Specifically, for the L-KDE baseline, we evaluate a Gaussian kernel with noise levels (standard deviations) of $\{0.01, 0.05, 0.1\}$. For the SR baseline, we consider intermediate times $\{0.1, 0.5, 0.9\}$. For simplicity, we only examine the scenario where there is a single guiding point (i.e., $\mathcal{X}_1^g$ and $\mathcal{X}_t^g$ are singleton sets). Each experiment is repeated with five

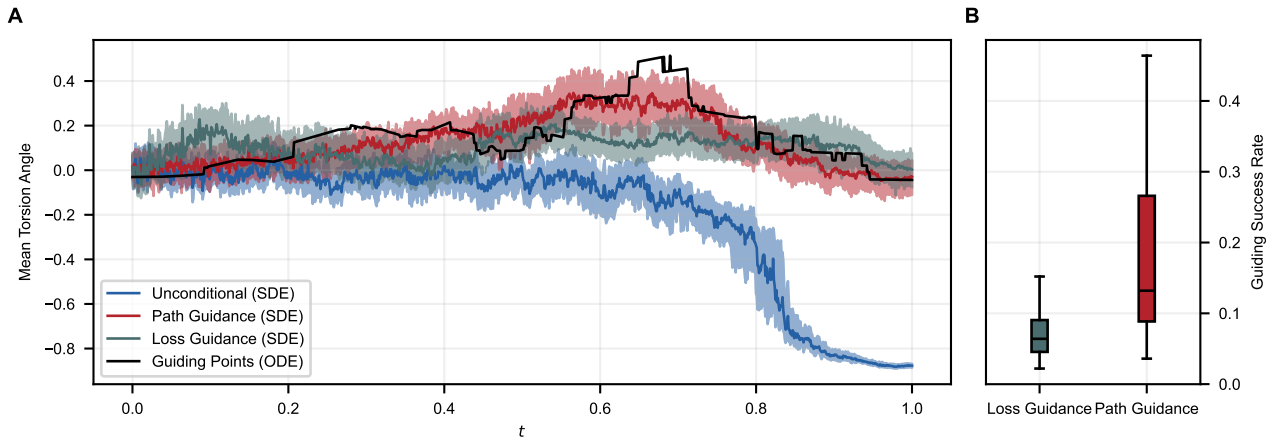

Figure 12: **Path Guidance vs. Loss-Guidance for sampling Transition States**. (A) Evolution of the mean torsion angle (which determines the state of the protein) during the diffusion process. (B) Guiding success rates across different parameter settings.

different seeds.

In the following figures (Figures Figure 13 – Figure 18), we provide various metrics, histograms, and energy surfaces that summarize the trends observed in these baseline guidance scenarios. Overall, the results strongly suggest that guidance biases the sampling procedure toward the reference guiding points, which aligns with our intuition.

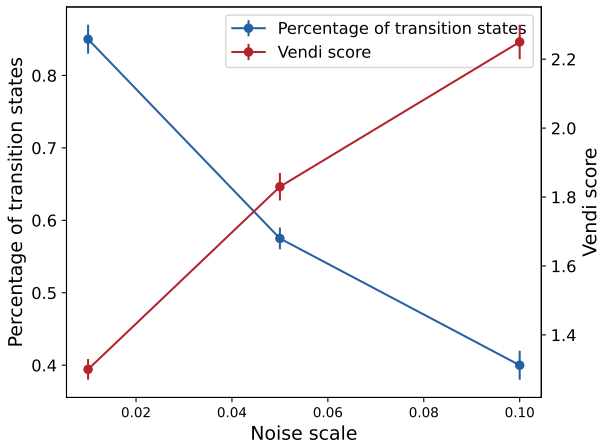

Figure 13: **Trade-off between sample variance and guidance success rate (L-KDE).** As the KDE noise scale increases for the L-KDE baseline, the percentage of transition states among the generated samples decreases (blue), while the vendi score among the generated states increases (red).

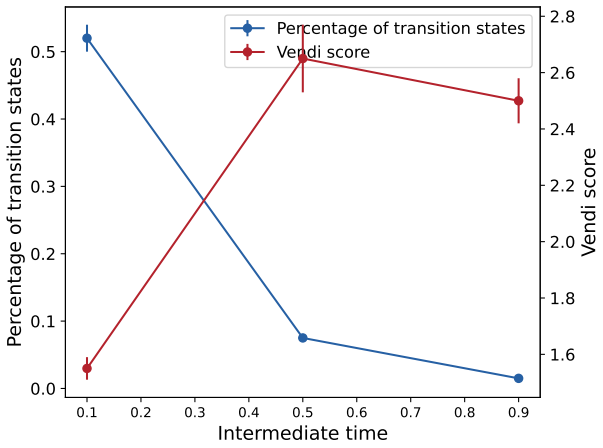

Figure 14: **Trade-off between sample variance and guidance success rate (SR).** As the selected time step t increases for the SR baseline, the percentage of transition states among the generated samples decreases (blue), while the vendi score among the generated states tends to increase (red).

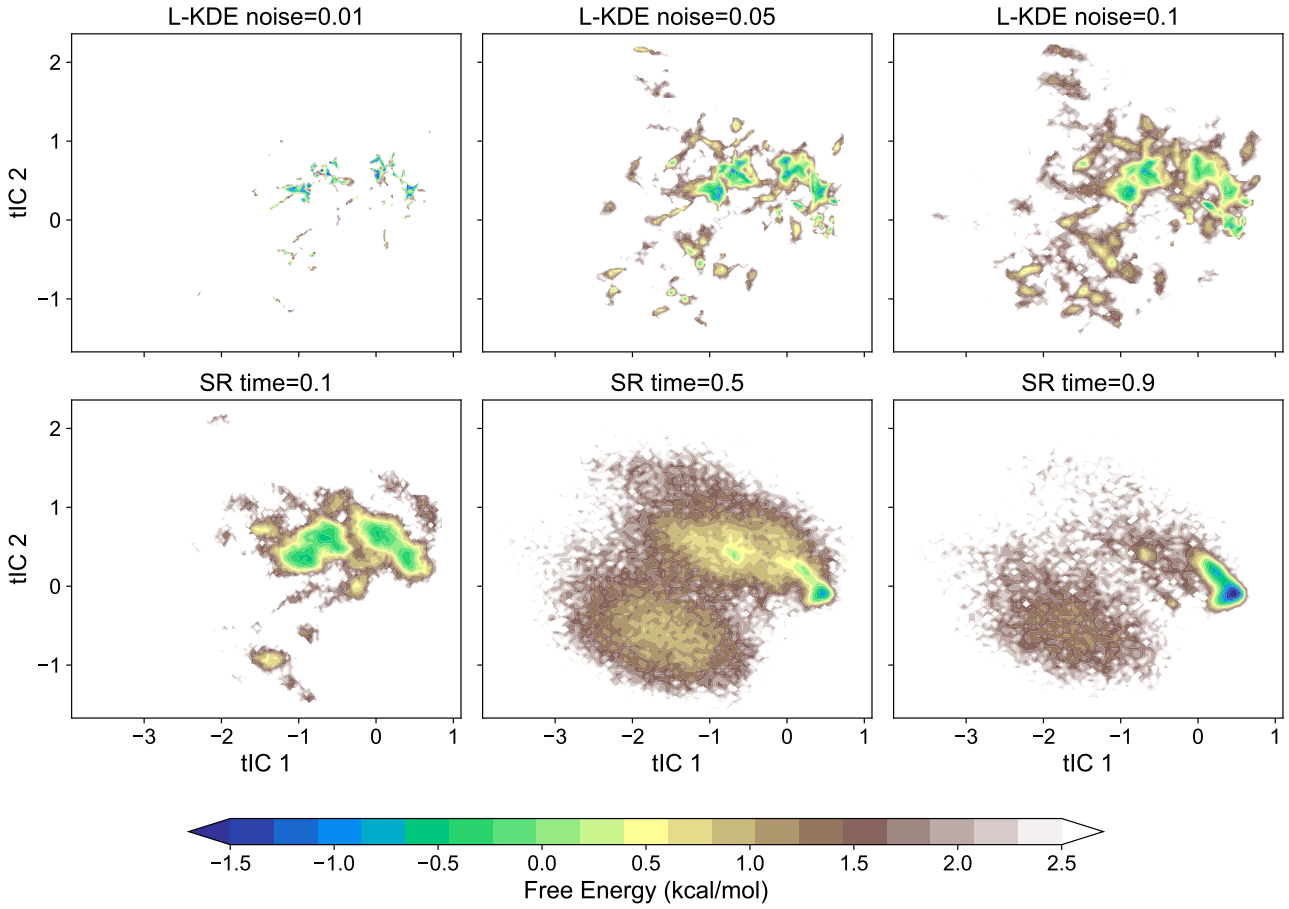

Figure 15: **Energy surface plots.** First row: L-KDE baseline for various levels of noise scale. The smaller the perturbation, the more concentrated the samples around the transition states region. Second row: SR baseline for various values of intermediate time. The smaller the stochasticity level, the more concentrated the samples around the transition states region. Compare with Figure 5 and Figure 3 A and B.

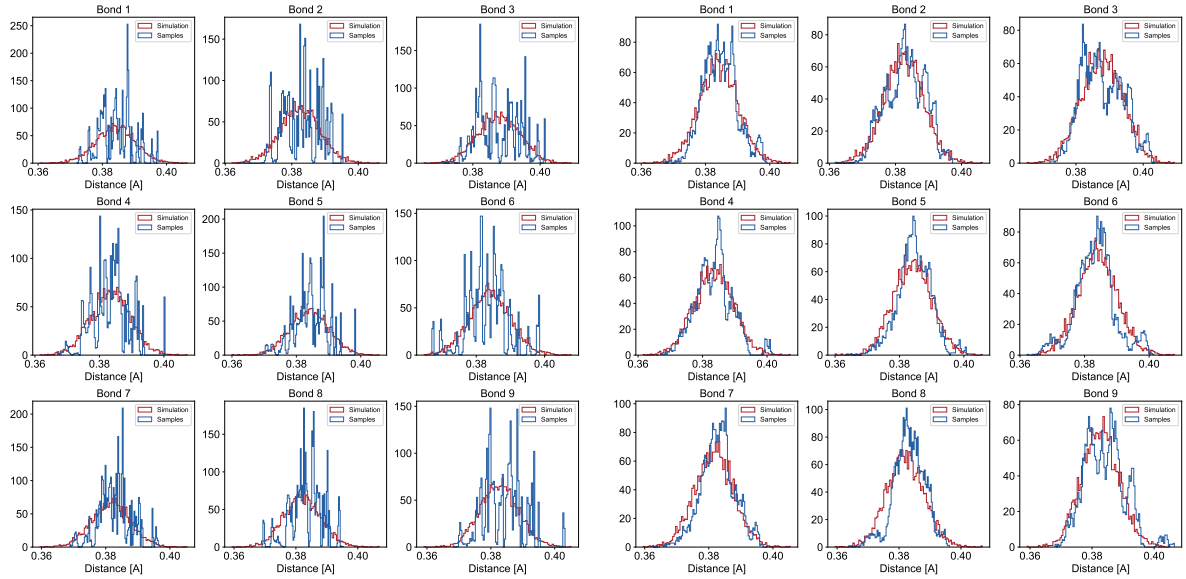

(a) L-KDE noise=0.01

(b) L-KDE noise=0.1

Figure 16: **Comparison of bond distance distributions for L-KDE and the reference.** The L-KDE baseline (blue) is superposed on the corresponding histogram of the unconditional (red) distribution (the CLN025 MD simulation). We see that for small perturbations, the generated samples seem to conform to particular details of the guiding samples. As the noise increases, the guidance impact diminishes. This is quantified in a more principled way in Figure 18.

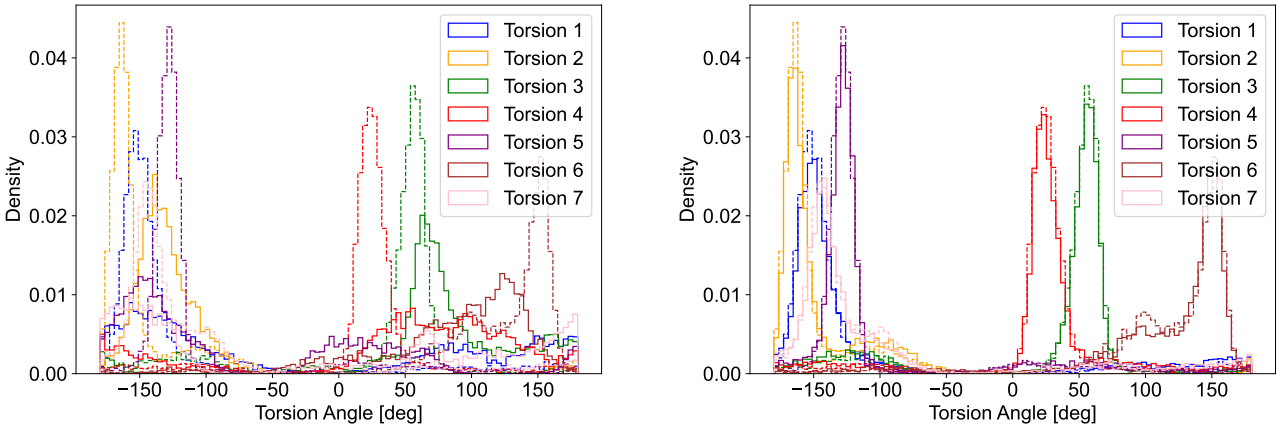

(a) SR intermediate time=0.1

(b) SR intermediate time=0.9

Figure 17: **Torsion angle histograms for the SR baseline at different noise levels.** Solid lines show SR samples at $t = 0.1$ (Left) and $t = 0.9$ (Right), superimposed on the corresponding unconditional distributions (dashed lines). At high stochasticity ($t = 0.9$), the torsion angle distribution becomes nearly indistinguishable from the unconditional one.

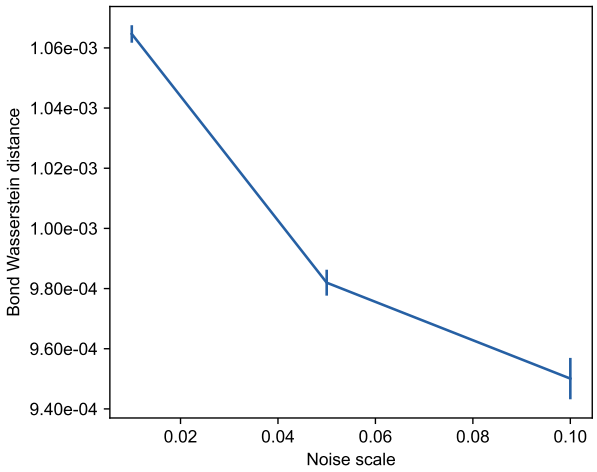

(a) Wasserstein distance vs noise scale for L-KDE baseline

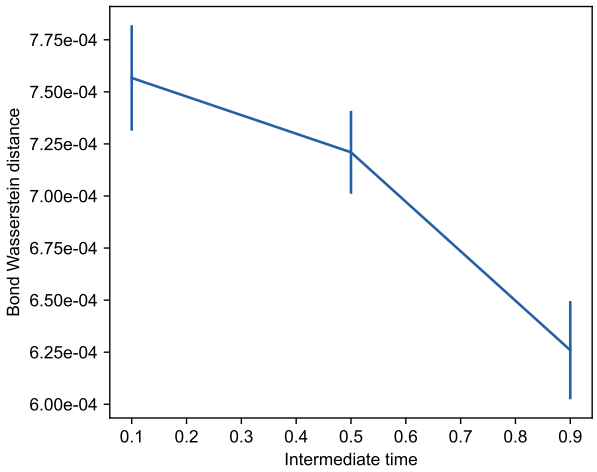

(b) Wasserstein distance vs intermediate time for SR baseline

Figure 18: **Wasserstein distance between baselines and reference bond distance distributions.** We measure the distance between the bond distance distributions of baseline methods and the CLN025 MD simulation (see Figure 16). As the stochasticity level increases for both baselines, the generated distributions converge toward the unconditional reference, indicating a reduced influence of the guidance signal.